

Combinatorial Screening of Nanoclay-Reinforced Hydrogels: A Glimpse of the “Holy Grail” in Orthopedic Stem Cell Therapy?

Masoud Hasany,^{†,‡,§} Ashish Thakur,[†] Nayere Taebnia,[†] Firoz Babu Kadumudi,[†] Mohammad-Ali Shahbazi,[†] Malgorzata Karolina Pierchala,[†] Soumyaranjan Mohanty,[†] Gorka Orive,^{||,⊥,♯} Thomas L. Andresen,[†] Casper Bindzus Foldager,[○] Soheila Yaghmaei,[‡] Ayyoob Arpanaei,^{§,ⓑ} Akhilesh K. Gaharwar,^{◆,¶,ⓑ,ⓓ} Mehdi Mehrali,^{*,†} and Alireza Dolatshahi-Pirouz^{*,†,ⓑ}

[†]DTU Nanotech, Center for Intestinal Absorption and Transport of Biopharmaceutical, Technical University of Denmark, 2800 Kgs, Lyngby, Denmark

[‡]Department of Chemical and Petroleum Engineering, Sharif University of Technology, P.O. Box 11365-11155, Tehran, Iran

[§]Department of Industrial and Environmental Biotechnology, National Institute of Genetic Engineering and Biotechnology, P.O. Box 14965/161, Tehran, Iran

^{||}NanoBioCel Group, Laboratory of Pharmaceutics, School of Pharmacy, University of the Basque Country UPV/EHU, Paseo de la Universidad 7, 01006 Vitoria-Gasteiz, Spain

[⊥]Biomedical Research Networking Centre in Bioengineering, Biomaterials and Nanomedicine (CIBER-BBN), 01006 Vitoria-Gasteiz, Spain

[♯]University Institute for Regenerative Medicine and Oral Implantology—UIRMI (UPV/EHU-Fundación Eduardo Anitua), 01007 Vitoria, Spain

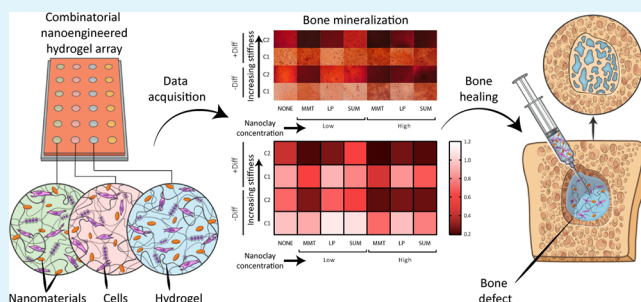
[○]Orthopaedic Research Laboratory, Department of Orthopaedic Surgery, Aarhus University Hospital, 8000 Aarhus, Denmark

[◆]Department of Biomedical Engineering, [¶]Department of Materials Science and Engineering, and [ⓓ]Center for Remote Health Technologies and Systems, Texas A&M University, College Station, Texas 77843, United States

Supporting Information

ABSTRACT: Despite the promise of hydrogel-based stem cell therapies in orthopedics, a significant need still exists for the development of injectable microenvironments capable of utilizing the regenerative potential of donor cells. Indeed, the quest for biomaterials that can direct stem cells into bone without the need of external factors has been the “Holy Grail” in orthopedic stem cell therapy for decades. To address this challenge, we have utilized a combinatorial approach to screen over 63 nanoengineered hydrogels made from alginate, hyaluronic acid, and two-dimensional nanoclays. Out of these combinations, we have identified a biomaterial that can promote osteogenesis in the absence of well-established differentiation factors such as bone morphogenetic protein 2 (BMP2) or dexamethasone. Notably, in our “hit” formulations we observed a 36-fold increase in alkaline phosphatase (ALP) activity and a 11-fold increase in the formation of mineralized matrix, compared to the control hydrogel. This induced osteogenesis was further supported by X-ray diffraction, scanning electron microscopy, Fourier transform infrared spectroscopy, and energy-dispersive X-ray spectroscopy. Additionally, the Montmorillonite-reinforced hydrogels exhibited high osteointegration as evident from the relatively stronger adhesion to the bone explants as compared to the control. Overall, our results demonstrate the capability of combinatorial and nanoengineered biomaterials to induce bone regeneration through osteoinduction of stem cells in a natural and differentiation-factor-free environment.

KEYWORDS: nanomaterials, nanocomposite hydrogels, nanoclays, cyborgamics, tissue engineering, osteoinduction, human mesenchymal stem cells, bone



INTRODUCTION

Bone fractures have become a major health issue worldwide, giving rise to chronic diseases involving fragility and pathological complications.¹ This trend is underscored by the fact that bone is currently the second most transplanted tissue

Received: July 11, 2018

Accepted: September 12, 2018

Published: September 18, 2018

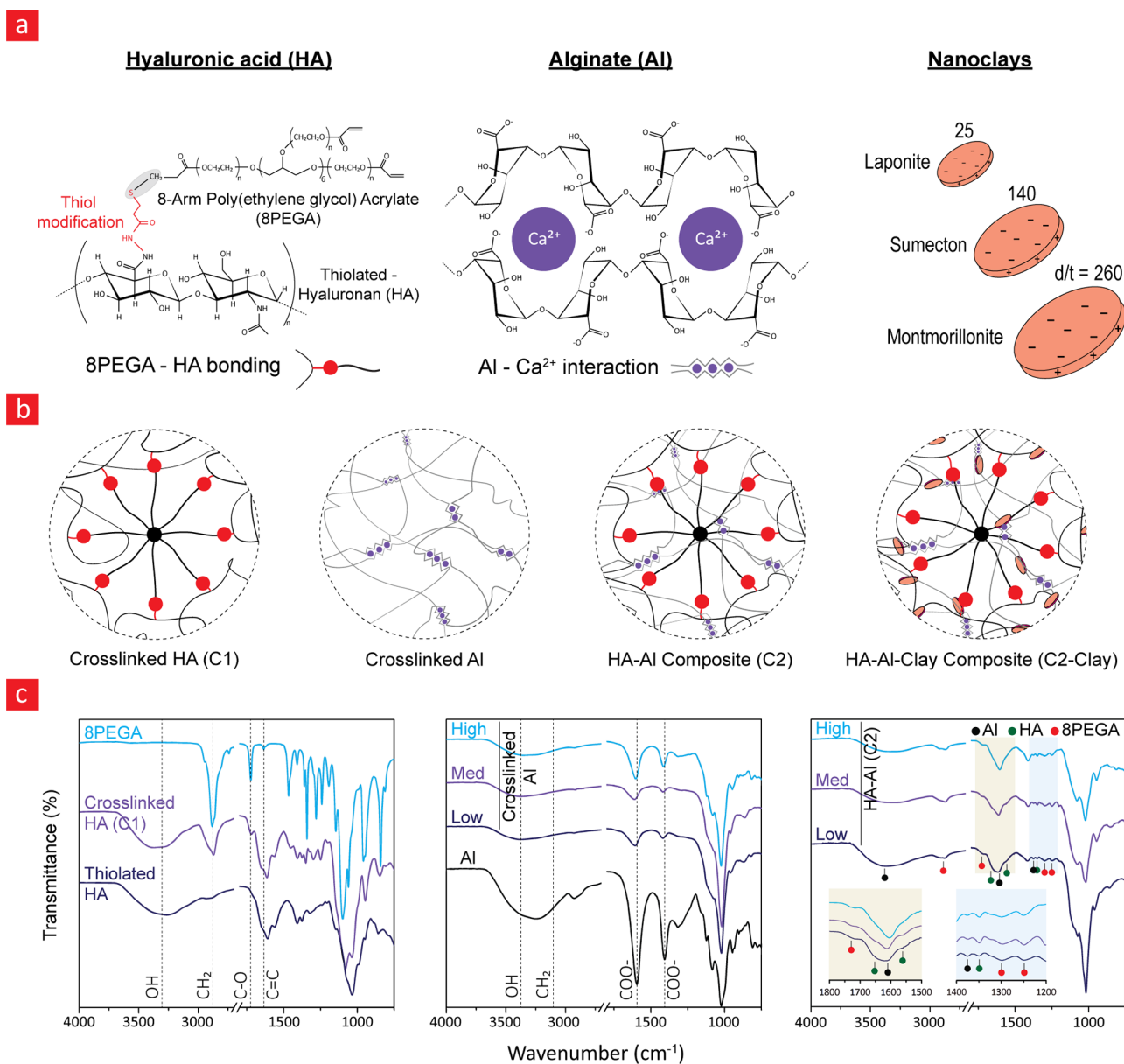


Figure 1. Chemistry behind the proposed cyborganic carriers and their characterization. (a) Chemical structures of hyaluronic acid (HA), 8-arm poly(ethylene glycol) acrylate (8PEGA), and alginate (Al) together with the dimensions of the various dual-charged clay nanomaterials used in this study. (b) Key principles behind the assembly of the hydrogels. (c) Fourier transform infrared (FTIR) characterization of the developed hydrogels.

in the world.² It is estimated that >50% of women and 20% of men aged >50 years will experience a bone fracture during the remainder of their lifetime. One promising strategy to remedy this situation entails syringe delivery of stem cells to the skeletal regions that are at high risk for fractures. To this end, recent studies in bone tissue engineering have highlighted the promise of such treatment methods to aid the patients suffering from bone disorders, including osteoporosis.^{3,4} However, a viable stem cell delivery system requires a carrier that can safeguard the cells from the disruptive shear forces during the injection phase;^{5,6} otherwise, the subpar number of surviving donor cells will limit the treatment efficacy of the therapy. At the same time, such systems need to retain the encapsulated cells within the targeted tissue and provide them with a stable three-dimensional (3D) environment to permit tissue repair and regeneration. Although using hydrogels to carry stem cells into the target site can address many of these

challenges,^{7–11} commercially available hydrogels are limited by their low mechanical stiffness and toughness.^{12,13} Consequently, they fail to withstand the *in vivo* mechanical forces for long time periods and instead disintegrate within the body.

Nanomaterials have emerged as promising biomaterial fillers with the ability to significantly improve the mechanical properties of biomaterials so they can meet the aforementioned requirements, while promoting osteogenic processes at the same time.^{13–20} They can also be used to engineer resilient and load-bearing hydrogels with formidable osteogenic capabilities^{18,19,21} and even used as potential stem cell carriers that can reorganize into premature cyborg-like tissues and organs (cyborganics) with the capacity to monitor, stimulate, and regenerate dysfunctional tissues.^{13,22–24}

Despite these advances, some of the current nanoengineered hydrogels are still not suited for load-bearing tissues (such as bone) due to their inherent mechanical weakness and low

durability in the body. The rigmarole of finding an optimal combination of nanopolymer- and biopolymer-based materials among a vast number of possibilities remains a primary challenge. This inherent conflict between combinatorial testing and scientific throughput has bothered scientists in the field of natural sciences throughout the ages.

To address this long-standing scientific challenge, we have utilized a combinatorial and high-throughput platform for time-efficient and low-cost development of optimal stem cell delivery systems. Specifically, we have developed a combinatorial library consisting of 63 hydrogels made from double-bonded polysaccharide-based hydrogels (containing ionic-covalent entanglement network) and multifunctional two-dimensional (2D) nanosilicates (namely, Laponite (LP), Sumecton (SUM), and Montmorillonite (MMT)) with an almost similar chemistry but different geometrical properties (Figure 1). We hypothesize that our combinatorial hydrogels can significantly enhance the carrier's mechanical properties without increasing hydrogel cross-linking and polymer density to a point that makes them useless for tissue engineering applications due to the associated decrease in hydrogel porosity and hydration degree. In addition, these hydrogels cross-link through simple one-step mixing procedures in contrast to many of their counterparts, which are solidified through complex and toxic chemical reactions.

Our results also demonstrate that these nanoengineered hydrogels can be fine-tuned into combinations that enable osteogenic differentiation of human mesenchymal stem cells (hMSCs) in differentiation-factor-free culture conditions. We have also demonstrated that the incorporation of the proposed multifunctional nanomaterials gives the hydrogels injectable, shock-absorbing, and osteogenic properties under conditions that do not compromise their biocompatibility. Our carrier system accordingly holds great promise as an advanced stem cell delivery system for treating bone disorders. Indeed, injectable and mechanically resilient 3D biomaterials that can transform stem cells into osteogenic cells without using expensive differentiation media are still in their infancy; nevertheless, they represent a glimmer of hope for the field of bone tissue engineering due to their long-term stability and capability to spontaneously direct donor cells into mature bone tissues within the body.

RESULTS

Hyaluronic acid (HA) is a negatively charged polysaccharide found in the extracellular matrix (ECM) of most human tissues.²⁵ It is widely used in the field of tissue engineering because it resembles native ECM and is capable of regulating cellular processes such as differentiation and proliferation.²⁵ Chemically, it is characterized by repeating subunits of disaccharides, D-glucuronic acid and N-acetyl-D-glucosamine, that are linked via β -(1 \rightarrow 4) and β -(1 \rightarrow 3) glycosidic bonds (Figure 1a).²⁶ A number of cross-linking protocols exist for transforming HA prepolymers into hydrogels. In this study, we used a well-established cross-linking method based on thiolated HA and 8-arm PEG-acrylates (8PEGA) that undergo Michael addition reaction to form a covalently bonded hydrogel (Figure 1a,b).²⁷ However, HA-based hydrogels are soft and break easily under load-bearing microenvironments. To address this limitation, we have combined HA (C1) with an ionically cross-linked alginate (Al) network to create a double-bonded and tough hydrogel.^{12,28} Additionally, we have nanoreinforced the HA-Al (C2)-based hydrogel with a library

of dual-charged clay nanomaterials, including Laponite (LP), Sumecton (SUM), and Montmorillonite (MMT). These nanoclays are unique in their geometrical aspects but retain comparable material properties and composition (silicate, magnesium, lithium, and/or aluminum) (Figure 1a).¹³ In the following sections, we characterize the above-mentioned combinatorial hydrogel libraries in terms of the underlying chemistry behind their cross-linking, as well as their three-dimensional (3D) morphology, hydration properties, structural integrity, and degradation profile. Subsequently, we demonstrate the biological performance of our proposed hydrogel for tissue engineering application.

Chemical Characterization. Fourier transform infrared (FTIR) spectroscopy was utilized to characterize the chemical structures of HA, Al, 8PEGA, and the cross-linked composite hydrogels (Figure 1c). The HA-8PEGA hydrogels were formed by the interaction between 8PEGA vinyl groups and the thiol groups of the HA in a "click" thiol-ene reaction.²⁹

The hydrogel gelation time upon 8PEGA addition to the hydrogel presolution was approximately 350 s. During this time period, the hydrogel presolution also exhibited shear-thinning properties and is thus also injectable in the sense that it can readily be injected when exposed to sufficient shear forces, while at the same time, gradually transforming into a more solidlike hydrogel state (Supporting Information Figure S1).

¹H NMR analysis was performed to further confirm the thiolene reaction and describe important elements in the various components used in the manufacturing of our hydrogels (Figure S1d). Acrylate-based proton ¹H NMR (D₂O) peaks are observed at \sim 5.9, 6.1, and 6.4 ppm (3H, HC=CH₂) (peak (a)) together with a number of ¹H NMR peaks within the range of 3.4–4.3 ppm (peak (b)) associated with the polymeric backbone of 8PEGA.^{30,31} ¹H NMR (D₂O) peaks corresponding to the disaccharides of HA are also observed in the range 3.1–4.5 ppm, as well as a peak at 1.9 ppm related to the methyl group in the N-acetyl-D-glucosamine unit. Moreover, two important proton peaks at \sim 2.6 and 2.7 ppm (peaks (d) and (e)), which are associated to the adjacent alkyl groups in the thiol group (CH₂CH₂SH) of HA (carbon-carbon like bonds) are also evident from Figure S1d.³² The ¹H NMR spectrum of the HA-8PEGA on the other hand reveals a new proton peak associated with S-CH₂ at 2.8 ppm (peak (c)), which confirms the successful formation of a covalent bond between acrylate and thiol groups, on 8PEGA and HA, respectively.

The presence of 8PEGA within the gelified network was also confirmed via the FTIR spectra, as shown in Figure 1c. Peaks were observed for 8PEGA at 2872 cm⁻¹ (CH₂ stretching), 1720 cm⁻¹ (C=O stretching), 1298 cm⁻¹ (C-O asymmetric bending), and 1250 cm⁻¹ (C-O asymmetric bending).³⁰ Similarly, the presence of thiolated HA accounted for the broad peak at 3600–3000 cm⁻¹ (ν OH) and other observed peaks at 1651 cm⁻¹ (amide I), 1562 cm⁻¹ (amide II), and 1375 cm⁻¹ (amide III).³³ All HA- and 8PEGA-related peaks were observed in the cross-linked HA-8PEGA (C1) hydrogel spectra, and the absence of C=C (1636 cm⁻¹) bonds demonstrated covalent linkage between HA and 8PEGA.³⁴

In contrast, the Al hydrogels were immediately formed via ionic cross-linking in the presence of calcium chloride (CaCl₂). Figure 1c shows the FTIR spectra of non-cross-linked and cross-linked Al at various concentrations. The non-cross-linked Al shows asymmetric and symmetric stretching vibrations of

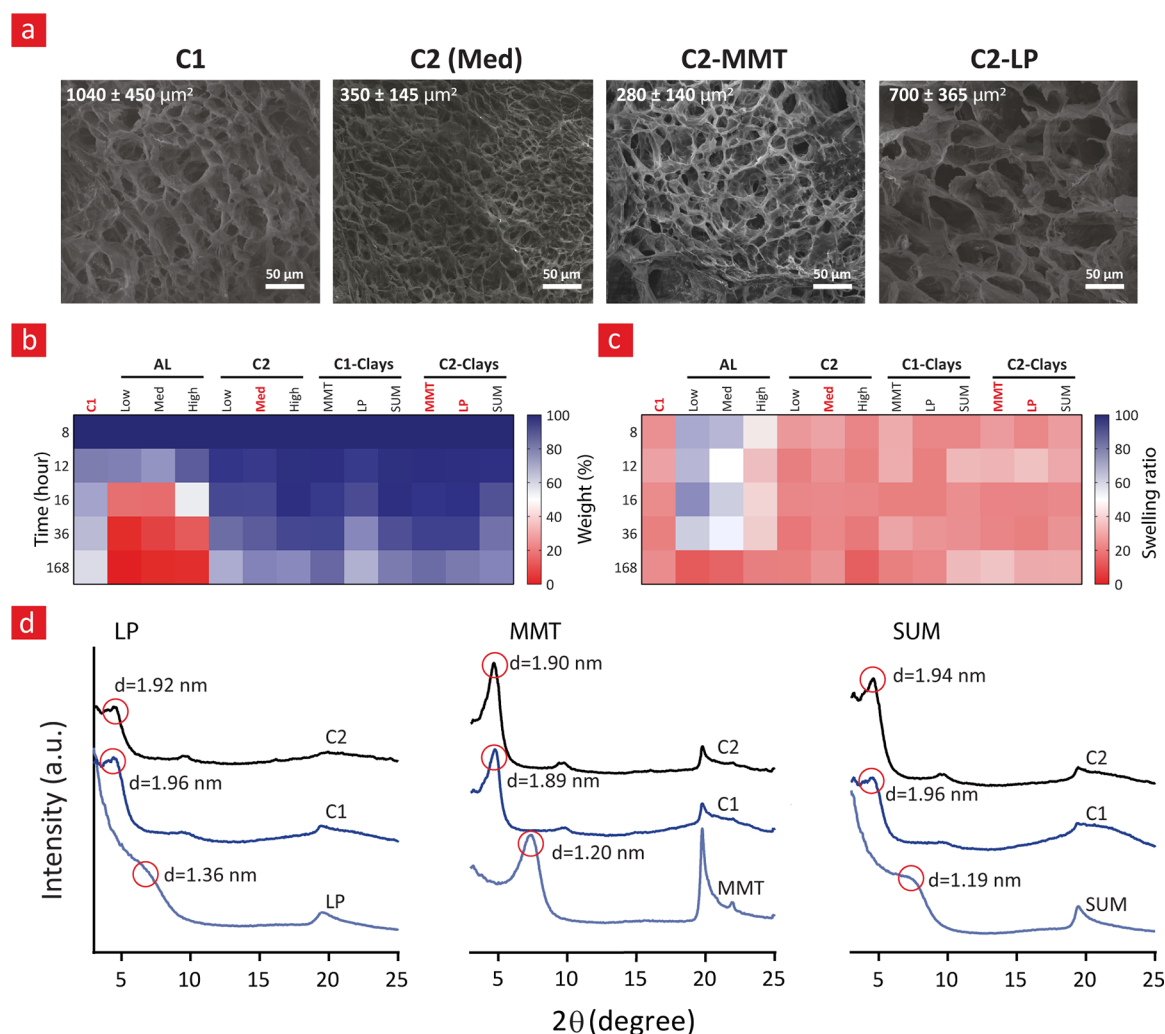


Figure 2. Porosity and stability studies. (a) Scanning electron microscopy (SEM) images of the developed hydrogels used as cyborganic carriers in the final stages of the study. (b) Combinatorial heat diagram showing the degradation profile of the hydrogels. (c) Combinatorial heat diagram showing the swelling properties of the hydrogels. (d) Degree of nanomaterial exfoliation within the hydrogels systems characterized by X-ray diffraction (XRD).

carboxylate (COO^-) ions at 1595 and 1407 cm^{-1} , respectively.³⁵ Upon cross-linking, these stretching vibrations shift to 1608 and 1419 cm^{-1} , respectively, suggesting the formation of an “egg-box” structure via the interaction between Ca^{2+} and COO^- .^{35,36} The formation of C2 composite hydrogel (HA–Al–8PGEA– Ca^{2+}) was confirmed by the presence of overlapping peaks from HA–8PGEA and Al– Ca^{2+} .

Finally, the chemical characteristics of the C2-clay hydrogels were also analyzed by FTIR spectroscopy (Supporting Information Figure S2). Nanoclays’ FTIR spectra showed the characteristic peaks corresponding to the stretching vibration of silicon oxide (Si–O–Si), silanol (Si–OH), and silicon monoxide (Si–O) in the range of 960 – 1120 cm^{-1} . The appearance of these characteristic peaks confirmed nanoclays’ presence within the C2 hydrogel composites.^{21,37}

Hydrogel Porosity, Swelling, and Stability Studies.

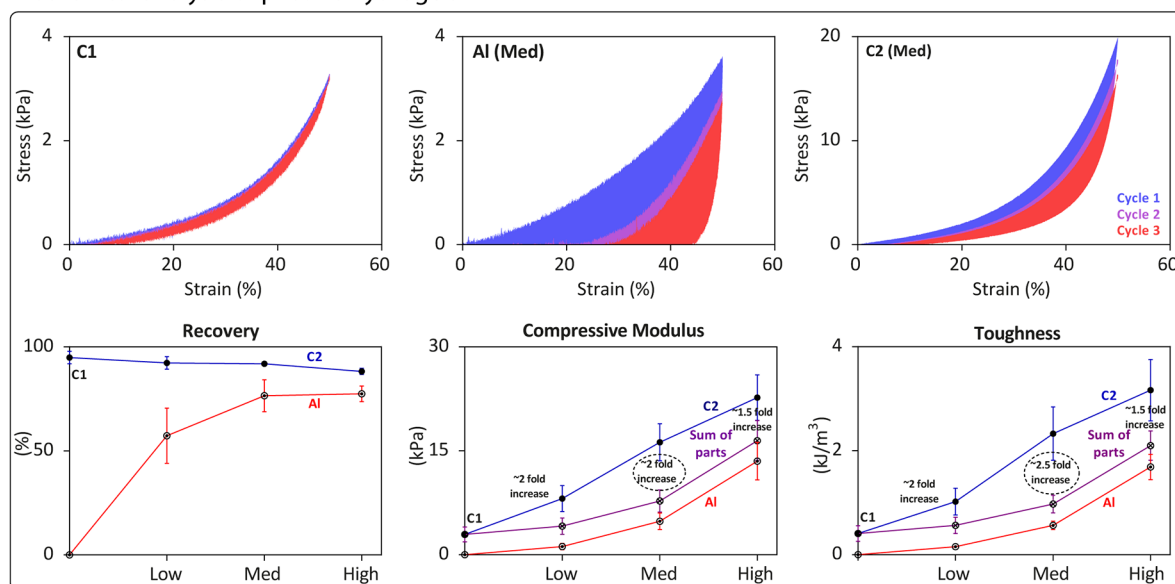
Long-term cell encapsulation should facilitate cell survival, proliferation, and differentiation. This requires an efficient transport of nutrients and metabolic waste products, which necessitates an interconnected hydrogel network with sufficient porosity (typically $>100\text{ }\mu\text{m}^2$).³⁸ For this reason, we used scanning electron microscopy (SEM) to characterize the

intrinsic nanoreinforced hydrogel morphology (Figure 2a). The SEM results suggested that hydrogel porosity tended to drop as nanoclays were added in accordance with a higher cross-linking density and mechanical integrity. Importantly, the pore area is sufficiently higher than $100\text{ }\mu\text{m}^2$ and therefore meets the requirement for efficient fluid exchange with the surrounding environment.

The degradation profile of the hydrogel library was examined to screen for the most stable hydrogels (Figure 2b). The results in Figure 2b demonstrate that Al hydrogels degraded completely after a few days of incubation, whereas the C1 and C2 hydrogels remained stable for longer duration. Specifically, the C2 hydrogels were slightly more stable than the C1 ones, and its stability further increased with the incorporation of nanoclay materials. Overall, the results displayed in Figure 2b indicate that Al hydrogels are not suitable for cell encapsulation studies because of their accelerated degradation dynamics, whereas the remaining hydrogel compositions meet the porosity requirements while exhibiting a sufficient physiological stability.

The combinatorial degradation studies were followed by combinatorial hydration studies as the native ECM micro-

a Mechanical analysis of pristine hydrogels



b Mechanical analysis of nanoreinforced C2 hydrogels

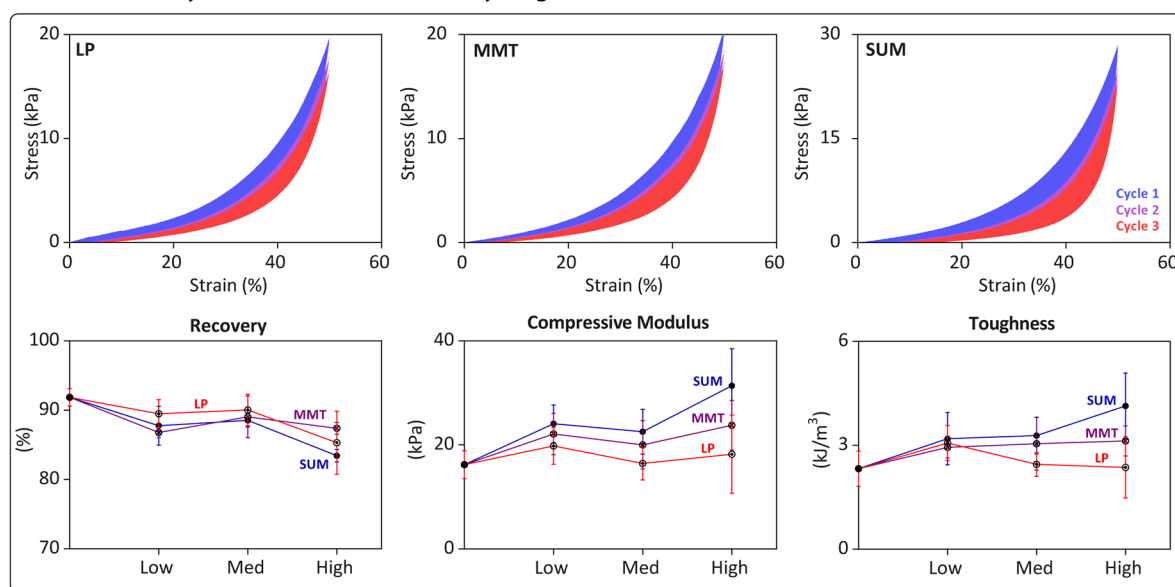


Figure 3. Mechanical analysis. (a) Stress–strain curves corresponding to the mechanical compression test assays done for HA (C1) and Al and HA–Al (C2) at different Al concentrations (low, medium, and high). Three cycles were run for each combination. The toughness values were retrieved from the area below the stress–strain curves and plotted here as a function of the Al content in the HA hydrogels. The compressive modulus was likewise retrieved from the stress–strain curves by fitting the curves with a linear equation in the 15–25% strain region. The differences in the ultimate stress between cycles two and three for the tested hydrogel combinations, in percentage, are plotted here and denoted as recovery. (b) Stress–strain curves corresponding to the mechanical compression test assays done for the C2-clay composites together with the associated toughness, compressive modulus, and recovery values.

environment is highly hydrated; for these reasons, if a hydrogel is not sufficiently hydrated, the cell viability might become compromised to an extent that renders the hydrogel useless for tissue engineering applications. Moreover, hydrated hydrogels enable a much more efficient nutrient and metabolic waste material diffusion. The hydration degree of the combinatorial hydrogels was determined via the swelling ratio (ratio between hydrated and lyophilized hydrogels) (Figure 2c). These results indicate that the Al hydrogel was significantly more swollen (50–60 at 8 h) than the other hydrogel compositions (30–40 at 8 h); however, the swelling ratios of the composites and HA

hydrogels were still within the range of many conventional hydrogel systems.³⁹

Finally, to investigate the stability and dispersion of the nanoclay materials within the hydrogel network, a series of X-ray diffraction (XRD) studies were performed (Figure 2d). These studies indicate that the nanoclays were almost fully dispersed within the hydrogels as the *d*-spacing peak of pristine LP (*d* = 1.36), MMT (*d* = 1.20 nm), and SU (*d* = 1.19) shifted in the XRD spectra of the composite hydrogels and was shifted toward higher values. This is a well-established indicator of the formation of polymeric networks around nanoclays as this phenomenon increases the characteristic crystal lattice spacing

of nanoclays.⁴⁰ These results also indicate the presence of electrostatic interactions between the negatively charged regions of HA–Al and the positively charged edges of the nanoclays (Figure 1a). The electrostatic interactions between nanoclays and the hydrogel backbone further corroborates with the observed ζ -potential increase upon the nanoclay addition to HA–Al prepolymer solutions (Supporting Information Figure S1).

In summary, our characterization studies confirmed that the developed hydrogels are sufficiently porous and hydrated to allow optimal cell encapsulation. While the Al-based hydrogel displayed an unfavorable degradation profile, the other hydrogels were physiologically stable for at least up to 7 days.

Mechanical Analysis. Hydrogels' mechanical properties are at the very heart of their successful performance within the load-bearing bone microenvironment. Specifically, the hydrogel needs to be sufficiently rigid (typically between 25 and 60 kPa) to support osteogenesis.^{41,42} We further screened our combinatorial hydrogel library to identify hydrogels with Young's modulus within the aforementioned range that would enable significant energy absorption without compromising the mechanical recovery during loading and unloading cycles.

Pristine hydrogels were evaluated in terms of compressive modulus, toughness, energy-absorbing capacity, and recovery after three cycles of loading and unloading (Figure 3a). Our initial mechanical studies showed that most of the gels broke in the range of 53–56% (data not shown). For this reason, we decided to use a 50% strain value for all of the cyclic loading studies performed herein. The energy absorbed during each loading and unloading cycle was calculated as the area under the stress–strain curve (also known as hysteresis area) and the recovery as the percentage decline in the ultimate stress from cycle 2 \rightarrow 3. The mechanical analysis clearly showed that the Al hydrogel is probably not suitable for further downstream studies because of its poor recovery during load-bearing cycles, as evidenced from the cyclic stress–strain curves (Figure 3a) and the calculated mechanical recovery. On the contrary, the C1 hydrogel returned completely to its original state after three cycles with a recovery of 95%. The total dissipated energy by C1 from mechanical cycles 1 \rightarrow 3 was, however, not that high (0.3 ± 0.1 kJ/m³). C2 also exhibited a good recovery (88%), albeit a bit lower than the recovery seen for C1, but the total energy dissipated was several-fold larger compared to C1, as evidenced from the hysteresis data. We also evaluated our hydrogels' compressive modulus (Figure 3b). While C1 and Al hydrogels exhibited low mechanical strength for bone tissue engineering applications, the compressive modulus of C2-med (16.2 ± 2.7 kPa) and C2-high (22.7 ± 3.3 kPa) was found to be optimal.

To further understand the higher-energy dissipation capacity of C2 relative to C1, we calculated the toughness (area below the stress–strain curve) of these hydrogels (Figure 3a). These data clearly show that C2s' toughness values were significantly larger than those of the C1s', with this difference increasing concurrently with Al concentration (low, medium (med), and high). Specifically, the toughness value increased by almost 770% from C1 to the C2 composite with a high Al concentration (C2-high). Of note, this difference in mechanical toughness between C1 and C2 is not simply additive as the corresponding toughness of its individual components were less than that of the composite. Indeed, as seen from the results in Figure 3a, the toughness value for C2-med is 2.5 times larger than the sum of parts for the C1 and Al toughness values. This

finding suggests that the energy dissipation mechanism of the reversible ionic bonds in the composite hydrogels is most pronounced in the C2-med system; therefore, this system is ideal from a biomechanical perspective, why we decided to focus on C2-med nanoreinforced hydrogels for the remainder of our studies. A thorough analysis of nanoreinforced C1 and Al hydrogels can be found in the Supporting Information (Figure S3). We also tested the mechanical properties of the C2 hydrogel with/without Ca²⁺ and found significant mechanical improvements after its inclusion, in accordance with the above-mentioned hypothesis, in which reversible ionic bonds play a dominant mechanical role in this system (Supporting Information Figures S4 and S5).

The cyclic stress–strain curve for the C2-med-clays is presented in Figure 3b, from which a higher hysteresis is observed in the different mechanical cycles compared to the pristine C2 hydrogels. The stress–strain curves in Figure 3b therefore indicate that the shock-absorbing properties of the nanoreinforced C2s can become even more enhanced through the addition of nanoclays (different concentrations were incorporated; low, medium (med), and high) in accordance with a number of recent studies.^{21,43} Interestingly, the mechanical recovery ranged from 83 to 90% (2 \rightarrow 3) and was thus almost unaffected by the nanoclay incorporation. By analyzing the area bounded by each cycle, it is possible to determine the energy dissipated in the different cycles, and therefrom, obtain an estimate of the total energy dissipated (sum of all cycles). From such calculations, it can be seen that C2-med-SUM (6 ± 1.3 kJ/m³) contributed the most to the shock absorbance reinforcement, while C2-med-LP (3.5 ± 1.4 kJ/m³) contributed the least, and the contribution from C2-med-MMT (4.6 ± 0.4 kJ/m³) being between the two. This is significantly higher than the total energy dissipated by C1 (0.28 ± 0.14 kJ/m³) and C2-med (2.609 ± 0.594 kJ/m³). The toughness and compressive modulus values for the SUM-reinforced C2s were also generally larger than their LP- and MMT-reinforced counterparts. Indeed, the compressive modulus for SUM-reinforced C2s increased concomitantly with increasing nanoclay concentration, reaching a value of 31.4 ± 7.2 kPa at the highest concentrations. This was 195 and 1060% larger than the compressive modulus for the pristine C2-med and C1 hydrogels, respectively, and a modulus increase was also seen for the LP- and MMT-nanoreinforced C2s going from 16.2 ± 2.7 to 18.2 ± 7.5 and 23.8 ± 4.8 kPa, respectively. However, one drawback of using higher nanoclay concentrations is the formation of nanomaterial agglomerates. This adverse phenomenon is clearly visible from the data in Figure 3b, since the data deviation in the displayed mechanical data grows with growing nanoclay concentrations. We therefore decided not to include these high concentrations in the downstream studies.

In summary, we have identified a number of C2-reinforced hydrogels that meet the requirements of hydrogels for bone tissue engineering applications in terms of compressive modulus. Importantly, these systems possess an incredible energy absorbance capacity while displaying a desirable mechanical recovery at the same time.

Human Mesenchymal Stem Cell (hMSC) Viability. As previously reported by our group and others, HA and Al hydrogels support high hMSC viability.^{44–46} However, hMSC viability within nanoclay-reinforced HA–Al hydrogels have not yet been studied. Even though several studies have reported on the biocompatibility of nanoclays, their toxicity nonetheless

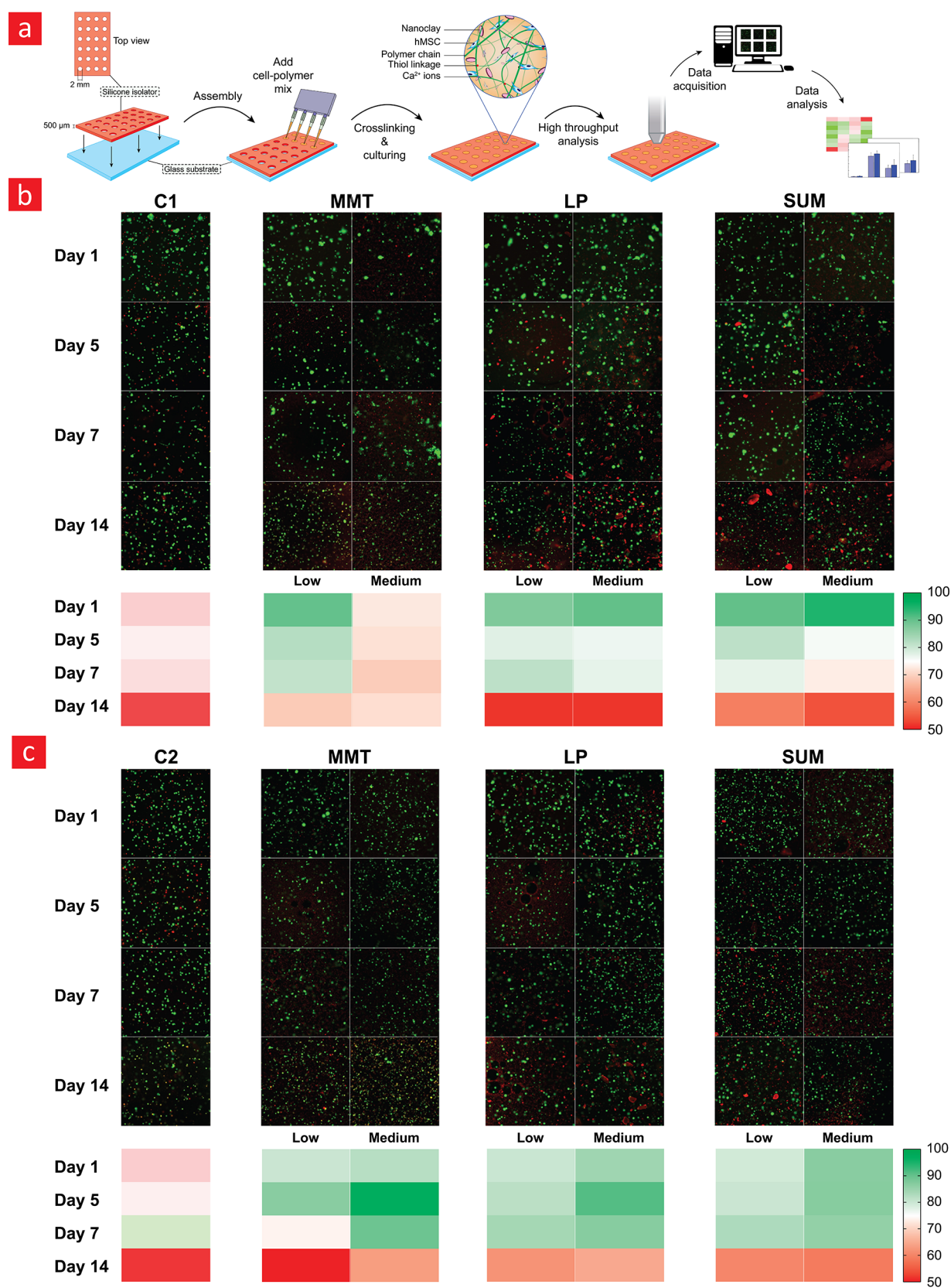


Figure 4. Human mesenchymal stem cell (hMSC) viability. (a) Schematic showing how the combinatorial hydrogel systems were assembled and examined through high-throughput data acquisition. The cell viability in hydrogels without (b) and with (c) alginate were determined from live (green)/dead (red) fluorescence imaging. The imaging experiments were performed after days 1, 5, 7, and 14, and the viability data retrieved from these fluorescence images were subsequently plotted in heat diagrams.

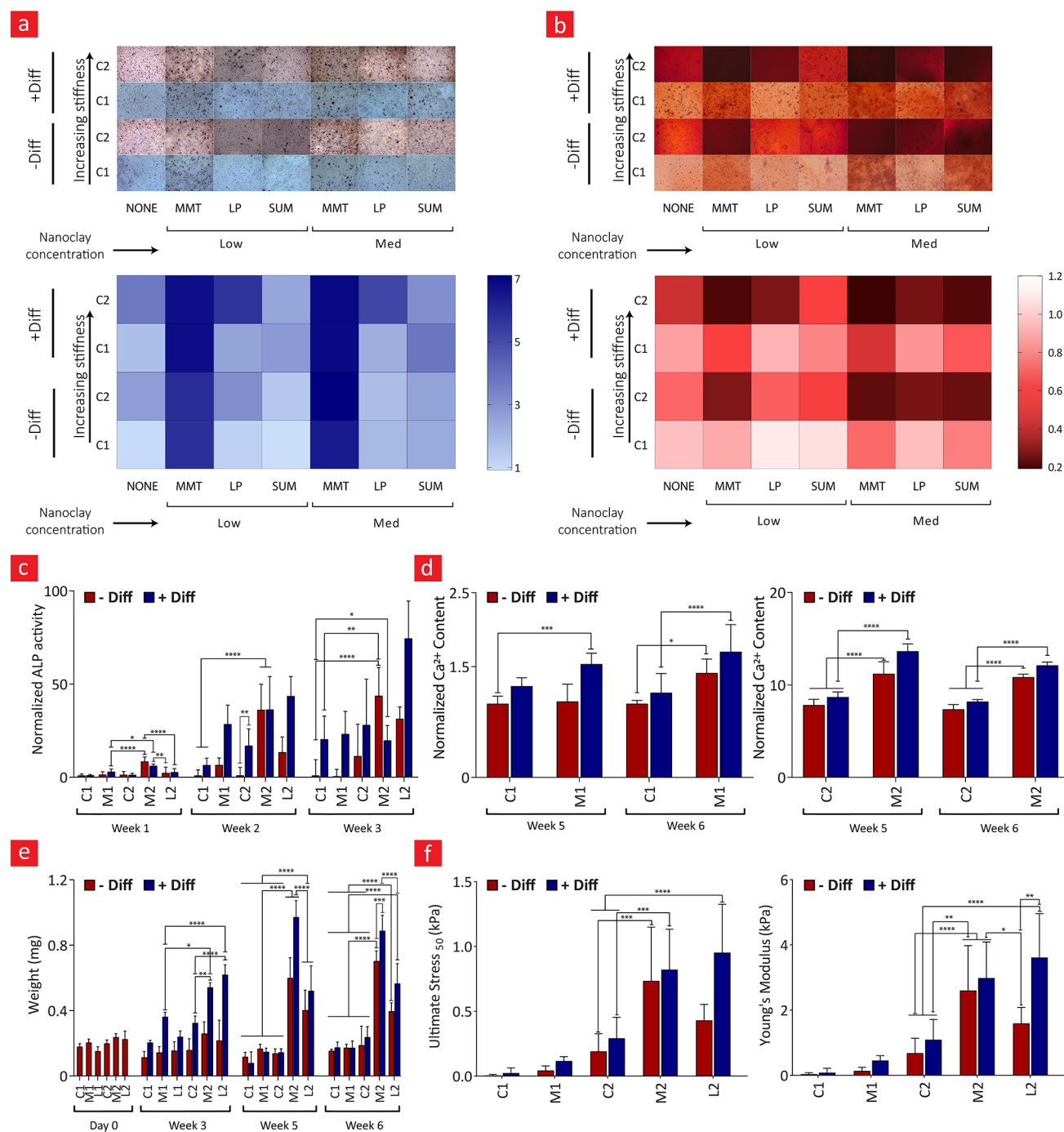


Figure 5. Osteogenic differentiation studies. (a) Alkaline phosphatase (ALP) images of the combinatorial composite systems. The amount of ALP (blue) was determined from image analyzer and plotted in a heat diagram. (b) A similar presentation of Alizarin Red S (Red) is shown here to give the reader an overview of how much calcium the hMSCs could generate during prolonged cultures within the developed hydrogel systems. (c) The ALP activity and (d) calcium content within the hydrogels were quantified with a spectrophotometer and plotted here. (e) Because of the really intensified mineralization process in some of the composites, the dry weight grew significantly in these systems over time. (f) Ultimate stress and Young's modulus of the hydrogels after 6 weeks of culture.

depends on the concentration and the type of hydrogel matrix.^{13,21,43,47} hMSCs biological behavior within the combinatorial hydrogels developed in this study is thus of broad interest to the field.

We have utilized our previous experience in high-throughput and combinatorial studies to test a repertoire of hydrogel combinations in a time-efficient and low-cost manner.^{45,48–51} Briefly, we have used an adhesive silicon-based hydrogel array to culture polymer-encapsulated hMSCs and analyze them in a

high-throughput manner by colorimetric live/dead stain and corresponding heat map representations (Figure 4a). These combinatorial data are presented in Figure 4b,c, in which we observed a high viability (>70%) on day 1 for all combinations, with the nanoreinforced hydrogels displaying the highest viability. This viability remained high (>70%) over the course of 7 days, but dropped significantly to approximately 50% in the pristine hydrogels on day 14 and on average 60–70% in the nanoreinforced hydrogel systems (Figure 4). Moreover, we

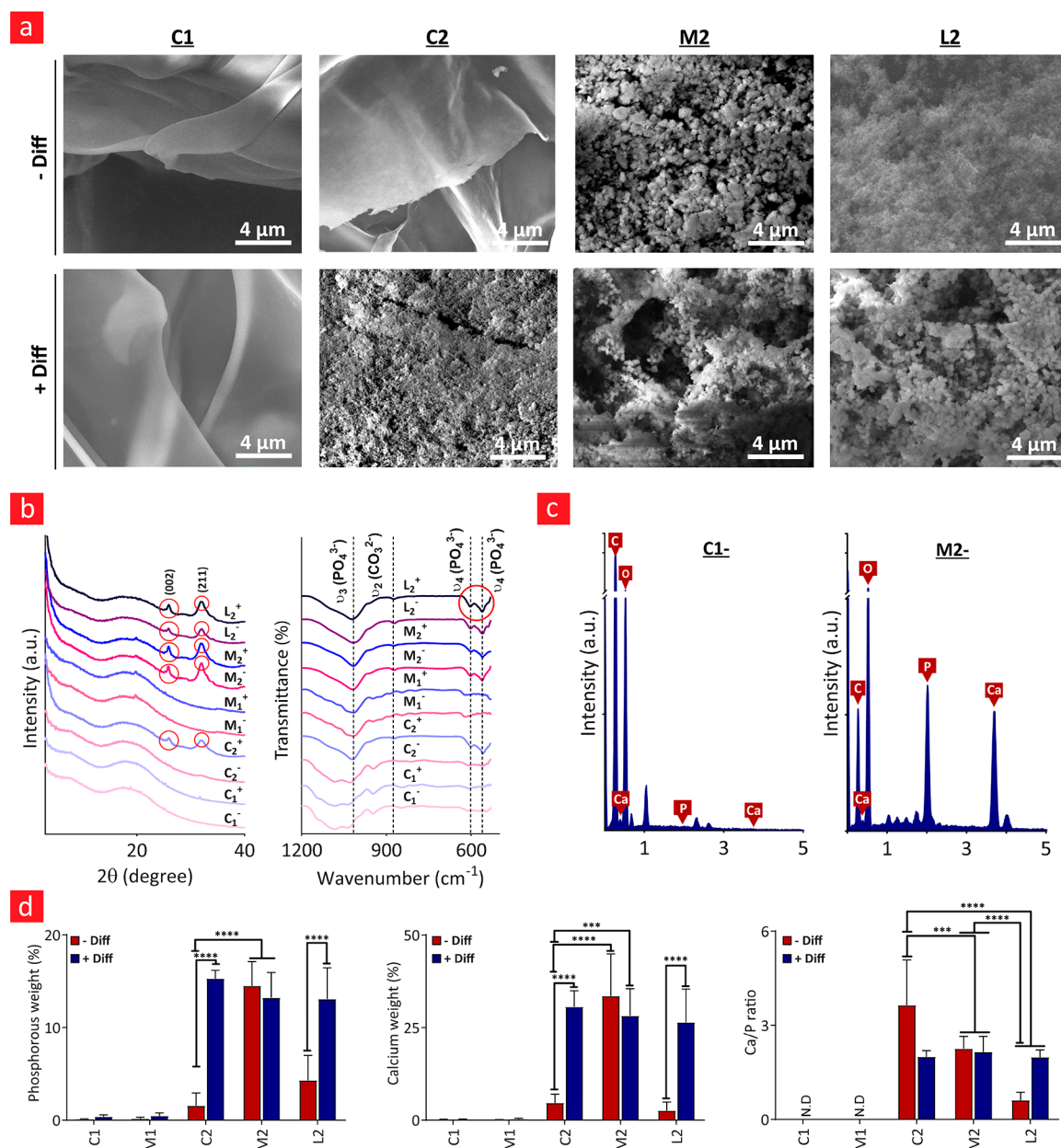


Figure 6. Mineralization studies. (a) Scanning electron microscopy (SEM) images of the hydrogels after 6 weeks of hMSCs culture. Nanometer-sized hydroxyapatite granules are visible from the SEM images corresponding to M2 and C2. (b) XRD and FTIR analyses of hydrogels after 6 weeks of hMSCs culture. Peaks corresponding to hydroxyapatite are marked with red circles. (c) Energy-dispersive X-ray spectroscopy (EDAX) was performed on the hMSCs-laden hydrogels after 6 weeks of culture to determine the amount of calcium (Ca) and phosphorous (P) generated by the hMSCs, since these minerals are the key ingredients in hydroxyapatite. (d) The amount of Ca and P was determined and displayed here. We also calculated the ratio between Ca and P as this ratio is a determining factor behind the purity of the generated hydroxyapatite.

also counted the cell nuclei by using a 4,6-diamidino-2-phenylindole dilactate (DAPI) assay and found a fairly even cell count in the respective hydrogel at around 50 cells per hydrogel (Figure S6), which was almost constant for up to 3 weeks of culture. Overall, these results suggest that nanoclays can improve encapsulated hMSCs' viability for extended periods of time.

Osteogenic Differentiation. The osteogenic differentiation potential of encapsulated hMSCs was tested within 28 hydrogels with the aforementioned combinatorial platform. Our assessment relied on the measured activity of alkaline phosphatase (ALP) and the degree of calcification via Alizarin Red S (ARED) staining. ALP is a glycoprotein found on the

surface of osteoblasts and is a sensitive and reliable indicator of bone metabolism,⁵² and ARED binds Ca²⁺, one of the major inorganic components of bone. The ALP and ARED stained hydrogels are shown in Figure 5a,b along with their corresponding normalized heat maps. These heat maps are based on the calculated ALP or ARED areas in the stained images, which subsequently have been normalized to the areas retrieved from the C1 hydrogel in normal culture media. In Figure 5a,b an increase in ALP and ARED expressions can be seen in the control and pristine C2 in differentiation media compared to the ones cultured in normal culture media. However, some of the nanoreinforced hydrogels, especially those based on MMT, not only exhibited a much higher

expression of the osteogenic markers compared to the pristine hydrogels, but could also induce these osteogenic marker profiles in normal culture media. However, this effect was moderately pronounced in LP-containing hydrogels and low in SUM-containing hydrogels. This qualitative analysis strongly suggests that MMT-containing hydrogels support osteogenesis even in a differentiation-factor-free environment. These results accordingly narrowed our investigation to MMT- and LP-containing hydrogels to further explore their prospects in bone tissue engineering applications. In the remaining part of this paper, these systems are referred to as L1, L2, M1, and M2, in which the numerals 1 and 2 refer to C1- and C2-reinforced hydrogels, respectively.

Next, we quantified the expression of ALP and formation of calcium deposits via colorimetric methods (Figure 5c,d). For all combinations, we observed increased ALP activity as a function of the hydrogel incubation time period. Notably, M2 hydrogels facilitated high ALP activity within just 1 week of culture in both differentiation (+) and normal (-) culture media. We did not observe any significant ALP upregulation in C1 and C2 in differentiation media after 1 week, which could indicate that ALP expression was below the noise detection level. Among all of the nanoreinforced hydrogels, M2 was the only one displaying an ALP activity that was significantly higher than C1+/- ($p < 0.0001$) and C2+/- ($p < 0.0001$) in this time period. Notably, M2 displayed a significantly higher ALP activity than C1 and C2 even in normal growth media in support of the conclusions drawn based on Figure 5a. Additionally, ALP activity of the M2-encapsulated hMSCs was also found to be significantly higher than that of M1 and L2 hydrogels in both types of culture conditions (Figure 5c).

This trend was also observed after week 2; however, the ALP activity in M1+ was found to be significantly higher than C1+/- ($p < 0.0001$) and C2- ($p < 0.0001$) but similar to the one measured in M2+/- and L2+/- . Likewise, ALP activity in L2+ was significantly higher than C1+/- ($p < 0.0001$) and C2- ($p < 0.0001$) and similar to M2+/- . We did not observe any significant ALP upregulation in C1+ hydrogels after 2 weeks; however, C2+ hydrogels showed significant ALP upregulation ($p < 0.05$) compared to C2-, possibly as a result of higher stiffness.

Similarly, in week 3, the ALP activity of hMSCs within the MMT-nanoreinforced hydrogels was found to be higher than the C2 and C1 hydrogels. Notably, while both LP- and MMT-containing hydrogels were able to promote ALP activity, the MMT-based hydrogels were the only ones able to do it in normal culture conditions in the absence of differentiation factors, which suggests that MMT hydrogels express intrinsic osteoinductive properties. To this end, we also observed that MMT facilitated a significantly higher calcium deposition in comparison to pristine hydrogels (C1 and C2) at weeks 5 and 6 (Figure 5d), which further bolsters the capability of osteoinduction of the M2 hydrogels to guide osteogenic hMSC differentiation.

Another hallmark for late-stage osteogenic differentiation is bone mineralization and the associated increase in the mechanical integrity and weight of the maturing bone tissue. To capture this interesting feature, we have measured the dry weights of the tested hydrogels (Figure 5e) at weeks 3, 5, and 6 in addition to their mechanical properties at week 6 (Figure 5f). We did not observe any significant differences among the dry weights of C1-, M1-, and C2- hydrogels; even though, the M1+ and C2+ hydrogels exhibited a significant weight

increase between day 0 and week 3; however, this significance disappeared at weeks 5 and 6, and in fact, a slightly lower weight was observed at these time points in line with a loss of mechanical integrity caused by a possible combination of low bone mineralization rate and high hydrogel degradation rates. On the other hand, the M2+/- and L2+/- hydrogels showed a significant and consecutive dry weight increase from day 0 to week 6, and for the most part, also a higher dry weight than the C1, M1, and L1 hydrogels. The weight increase in comparison to C1, M1, and L1 was most pronounced in the M2+ and L2+ hydrogels ($p < 0.0001$), and a significantly higher dry weight was observed for M2+ and L2+ hydrogels compared to M2- and L2- ($p < 0.0001$) at week 3. Furthermore, the M2+ hydrogels were significantly heavier than L2+ hydrogels at both weeks 5 and 6 ($p < 0.0001$ and $p < 0.0001$, respectively). On the basis of the findings presented in Figure 5e, it is plausible to assume that M2 hydrogels in general were more mechanically stable and heavier than the other combinations, possibly because of a more pronounced mineralization. This is supported by our mechanical analysis of the hydrogels at week 6, which demonstrates that the compressive Young's modulus and ultimate stress for the M2 and L2 hydrogels are higher than those of the M1, C2, and C1 hydrogels ($p < 0.0001$).

In summary, our in vitro analysis confirmed the effect of nanoreinforcements in upregulating hMSC bone differentiation. Particularly, our results strongly support the osteogenic potential of MMTs, as they were capable of facilitating hMSC differentiation in both normal and differentiating culture conditions.

Mineralization. To further investigate the mineral phase of the calcified matrix deposited by the hMSCs, we analyzed the hydrogels via SEM (Figure 6a). From these images, it was clear that temporal mineralization led to the formation of particles in M2+/-, C2+, and L2+/-, with visual appearance of hydroxyapatite ($\text{Ca}_5(\text{PO}_4)_3(\text{OH})$), the primary inorganic component of native bone. Contrastingly, the M1+/- (data not shown), C1+/- and C2- did not show the presence of such granulate features. To validate our hydroxyapatite theory, we analyzed the mineralized samples using XRD and FTIR (Figure 6b). From the XRD results, we observed two important hydroxyapatite-related peaks associated with the (002) and (211) crystalline planes of hydroxyapatite⁵³ in the M2+/-, L2+/-, and C2+ samples. The prominence of these peaks was higher in M2+/- and L2+ hydrogels, suggesting a higher degree of mineralization. Similar trends are evidenced by the FTIR spectra upon examining the $\nu_4(\text{PO}_4^{3-})$ peak, which is a well-established FTIR-related evidence for the presence of hydroxyapatite.⁵⁴

To back up our conclusions from the previous paragraph, we conducted out a series of supporting experiments on cell-free systems to confirm that most of the postulated hydroxyapatite formation was indeed facilitated by the hMSCs (Supporting Information Figures S7–S9). The hydroxyapatite-associated FTIR peaks seen in Figure 6 either were not present or less prominent (only C2 systems) in these studies and thereby fully supports the above-mentioned claims (Supporting Information Figures S7 and S8). The SEM images presented in Supporting Information Figure S9 also further validate these claims, as granulates and calcium/phosphate were not observed here. The nonprominent peaks in the FTIR spectra could therefore easily correspond to a possibly less pronounced hydroxyapatite formation caused by the presence of calcium, chlorine, and phosphorous, which are important components in simulated

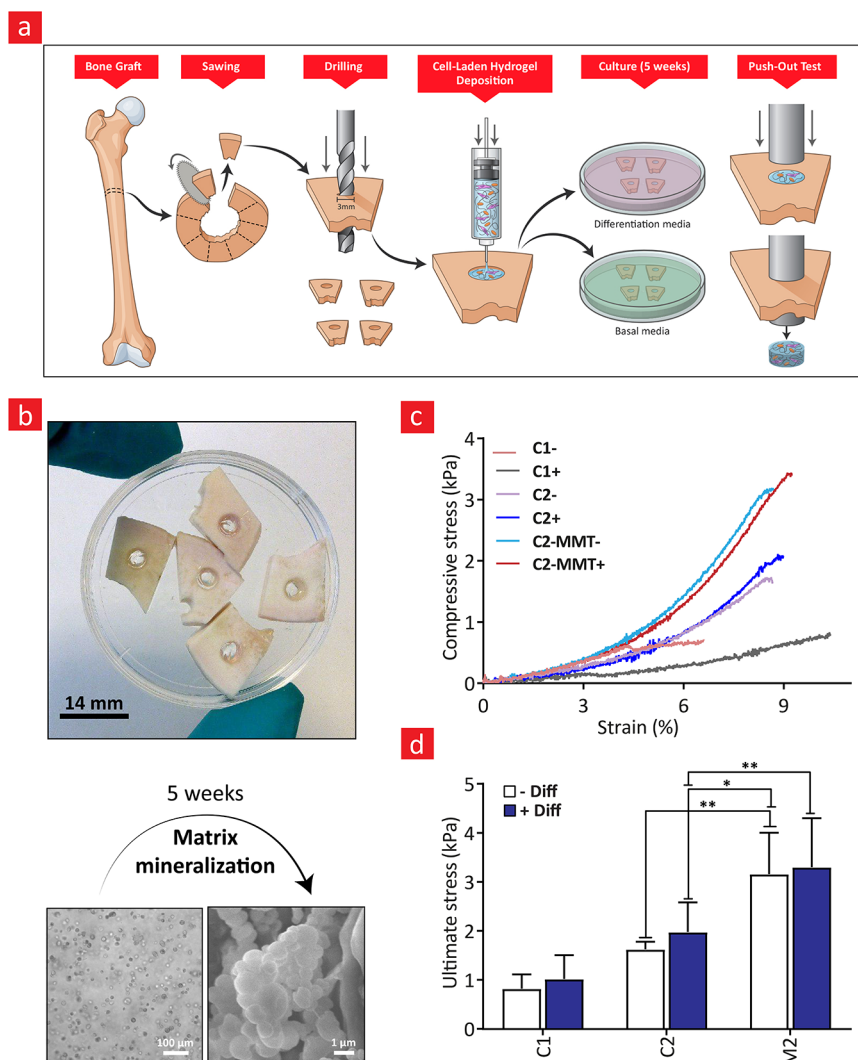


Figure 7. Push-out test. (a) Schematic showing how the ex vivo push-out test was performed. (b) Photographic and microscopic images of cell-laden hydrogels deposited in the artificial defects. Hydroxyapatite granules are visible from the SEM image corresponding to M2 sample. (c, d) Compressive stress–strain curves and the ultimate stress of deposited hydrogels after 5 weeks of culture.

body fluid (SBF) in the C2 hydrogel systems. This assumption is supported by some recent studies showing that MMT can facilitate hydroxyapatite formation in the presence of simulated body fluids (SBF) under cell-free conditions,⁵⁵ and some studies even show that SBF alone can do this.⁵⁶

To follow up on these results, we also analyzed the chemical composition of the hydrogels via energy-dispersive X-ray spectroscopy (EDAX) analysis (Figure 6c). The EDAX analysis further supported the presence of apatite minerals in these hydrogels (Figure 6c) due to the presence of calcium and phosphorous. To this end, the percentages of calcium and phosphorous in the various samples have been quantified and are presented in Figure 6d to determine the degree of mineral deposition in the respective hydrogels. These results demonstrate that the accumulation of calcium and phosphorous was almost nonexistent in the C1+/-, M1+/- and C2-, with the occurrence of small weight percentages in C2+ and L2-, while a significant difference was seen among the M2+/-, C2+, and L2+ hydrogels and the C1+/-, M1+/-, and C2- hydrogels ($p < 0.0001$ – 0.001). Notably, large calcium and phosphorous accumulations were seen in M2 in both differentiation and growth media. This was not the case for

C2 and L2, which strongly support the capacity of MMT to catalyze the formation of nativelylike hydroxyapatite without the aid of external osteogenic factors. We will thus solely focus on the M2-nanoreinforced hydrogels in the remaining sections of this paper.

Push-Out Test. Push-out tests are widely used in orthopedics to estimate the bone-biomaterial interfacial adhesion strength.⁵⁷ A strong adhesion between bone and biomaterial is essential for a long-term performance of the implant, which also indicates a successful fusion of the native bone with the artificial implant. We tested the capacity of M2 hydrogels to interface with the natural bone by injecting the cell-laden M2 polymer into the site of an artificial defect created within bovine bone explant, followed by a mechanical push-out test (Figure 7a,b). The hypothesis is that M2 would show a much better adhesion to the bone grafts due to its amazing ability to generate hydroxyapatite granules and much better mechanical integrity than C1+/- and C2+/- . Indeed, our results demonstrate a higher degree of osteointegration of the M2 hydrogels compared to the others, as evident from the larger compressive stress required to push them out of the bone explants (Figure 7c). This trend is clearly

visible in Figure 7d, from which a significantly higher ultimate stress was found for the M2 hydrogels as compared to the C1 ones ($p < 0.05$). Moreover, no significant difference was found between the C1 and C2 hydrogel groups, which clearly supported the M2 hydrogels' superior ability to mineralize and fuse with native bone.

DISCUSSION

The development of combinatorial hydrogel carrier systems for stem cell delivery requires multifunctional components and a high-throughput platform for rapidly selecting the right hydrogel ingredients for more detailed studies in a cost-effective manner. We have accomplished this by utilizing a combinatorial approach to deposit cell-laden hydrogels within microwells, however, first, we had to identify a suitable hydrogel library with sufficient mechanical integrity and long-term physiological stability to enable hMSC encapsulation and osteogenic differentiation.

In this regard, it was found that the combination of HA and AL (C2) was required to yield hydrogels that were stable enough under physiological conditions, sufficiently rigid, and capable of dissipating energy without compromising their mechanical recovery. Notably, we discovered that the toughness of C2 hydrogels was ~ 2.5 times greater than the sum of its individual (HA and Al) components. We believe that this phenomenon is a consequence of the double-bonded nature of the C2 composite, which consists of weak reversible ionic bonds (Al) and strong irreversible covalent HA polymer linkages. Numerous studies have shown that such mixtures of reversible and irreversible cross-links can generate mechanically tough and strong hydrogels.^{12,58} Furthermore, it is interesting to note that the superior mechanical properties resulting from such composite hydrogels are completely independent of the polymer concentration and the number of hydrogel cross-links. Indeed, the transfer of such superior mechanical properties to conventional hydrogels requires increasing the cross-linking density to an extent that renders them practically inapplicable for tissue engineering because of the associated decrease in hydrogel porosity and the therefrom significantly limited nutrient transport through the hydrogel.

The addition of nanoclay materials further enhanced the mechanical properties of C2 hydrogel in terms of its stiffness and energy-dissipating properties, and even though its mechanical recovery was slightly diminished, it was still sufficiently high ($>83\%$). This is likely due to the viscoelastic properties of nanoclays and their subsequent movement within the hydrogel under load-bearing conditions. Under normal circumstances, these dissipating mechanisms will fail, resulting in a nonrecoverable mechanical damage. The superior energy dissipation in C2-nanoclay hydrogels could be attributed to electrostatic interactions between the nanoclays and polymer components (HA and Al), as the positively charged rim of the nanoclays and the negatively charged groups in HA and Al can assemble into geometries that enable a recoverable hydrogel dynamics to yield a system that can sustain itself even if cross-links are broken during high strains.⁵⁹

Our interest in the research and development of stem cell carriers for treating bone disorders prompted us to carry out a number of osteogenic assays on the most promising hydrogel constructs. These hydrogels consisted of a combination of polysaccharides and various clay mineralites. Therefore, one could argue that the chemistry between C1 and C2, L1 and L2, and M1 and M2 was essentially the same, while the mechanical

properties for the 2's were higher than for the 1's due to the nature of their double bonds. Any biological differences seen between the respective hydrogels should therefore be attributed to either different mechanical properties or the presence of clay mineralites. Along these lines, we have observed significantly higher osteogenesis in C2 (22.7 ± 3.3 kPa) compared to C1 (3 ± 1 kPa) in terms of the measured ALP activity, calcification, and hydroxyapatite formation. Likewise, significantly higher osteogenesis was observed between the nanoreinforced C2's and C1's. On the basis of the discussion above, the most plausible factor behind these differences is a mechanical one. On the other hand, the improved osteogenic properties of M2 compared to L2 could be attributed to a higher mineral content in the former due to the larger volume of the MMT clays in addition to the observed higher compressive modulus of M2 hydrogels.

The biological results reported in this study are similar in many ways to other reports in the field. For instance, a number of studies have shown that Laponite can promote osteogenesis in an osteoinductive environment.^{18,19,21,47,49} However, biological studies with SUM are almost nonexistent, while some recent studies have demonstrated that MMT-reinforced 2D silk-based⁶⁰ and polyamidoamine-based substrates⁶¹ can upregulate the osteogenic fate of cells in osteogenic differentiation media. To this end, it is important to note that we have shown that MMT-reinforced and injectable composite hydrogels can promote osteogenesis of 3D encapsulated stem cells in a differentiation-factor-free environment.

It is plausible to assume that the observed osteogenic enhancement in the nanoreinforced C2 hydrogels could be caused by an intensified mechanotransduction between hMSCs and the hydrogel matrix due to a higher interfacial stiffness,^{41,42} in combination with a higher mineral content in the hydrogels.¹³ The link between mechanically induced osteogenesis and substrate stiffness is a well-studied one in the field as is evident from the decade-long research in this regard. We therefore will mainly discuss the relationship between osteogenic differentiation and mineral stimuli from the surrounding environment. In this direction, a number of studies in the field have shown that various clay minerals can supplement bone differentiation in the absence of growth factors.^{13,62} This is due to cellular ingestion of the clay particles and their subsequent breakdown into ionic products, such as lithium, magnesium, and silicate,^{13,62} which have been shown to interact with regulatory elements of osteogenic differentiation.^{63–65} Another essential product of clay disintegration, orthosilicic acid (H_4SiO_4), has been studied as an important factor involved in bone formation and bone maintenance. Examples include a number of groundbreaking studies that date back to the 1970s, which have linked silicate deficiency to various skeletal abnormalities and osteoporosis.^{66,67} Besides these landmark achievements in orthopedics, some recent studies have also shown that orthosilicic acid can promote bone mineralization, ECM matrix turnover, as well as important osteogenic pathways in preosteoblast cells.⁶⁸ On the basis of the results reported in this study and the current consensus in the area, we can conclude that hMSCs can be directed into bone cells in a differentiation-factor-free environment if they are cultured within microenvironments that provide the right combinatorial stimuli in the form of polysaccharides, sufficient mechanotransduction, and upregulation of intracellular mineralites.

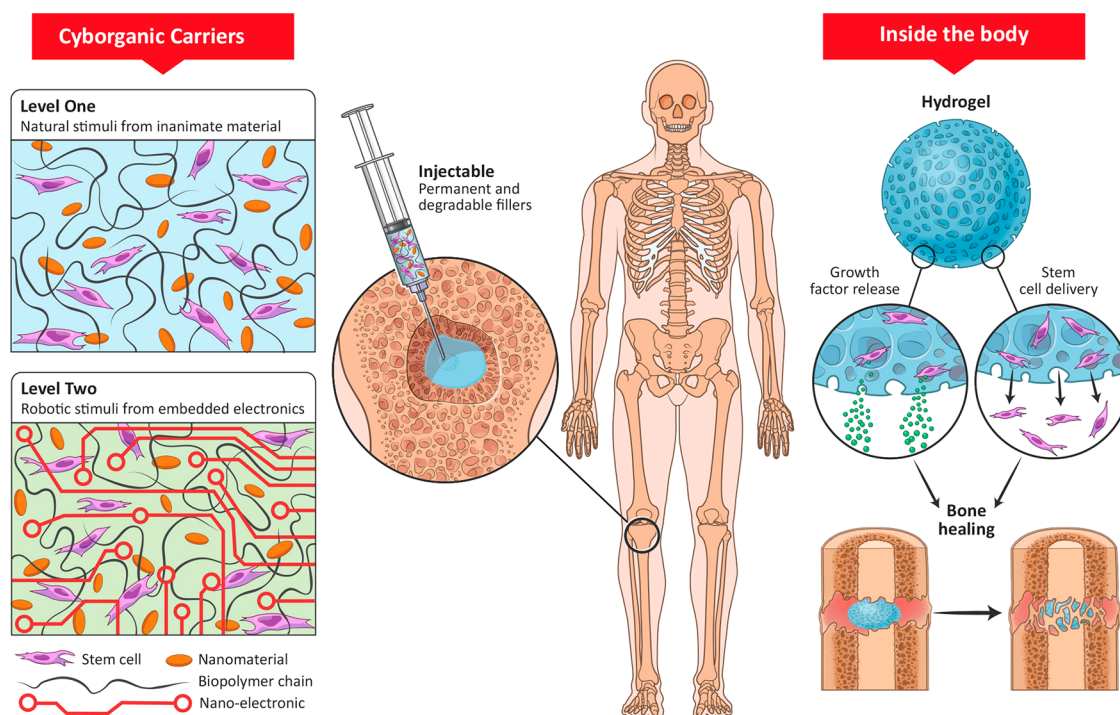


Figure 8. Schematic showing the key concepts behind cyborganic carriers for bone tissue engineering applications.

In Perspective. Tissue engineers have rapidly picked up injectable and nanoengineered biomaterials that combine living matter with inanimate materials to push regenerative therapies to a new level. For instance, a number of breakthrough studies have merged cell-laden hydrogels and nanomaterials to uncover a host of new constructs in the form of cyborg organic (cyborganic) carriers.^{13,62} These half-living organs and half-machine-like systems previously emphasized in the world of fantasy and fiction are now gradually becoming a part of mainstream science. The cyborganic carriers form two categories (Figure 8): (1) those that utilize the multifunctionality of nanomaterials to enhance tissue functionality and maturation^{13,18,19,21,69} and (2) those that combine nanomaterials and cells into meshes consisting of living tissues and bioelectronics.^{13,22–24,70} Level one cyborganics are currently the ones that have been studied the most in the context of facilitating tissue regeneration, or indirectly by turning into “cyborganic factories” that produce regenerative growth factors and new stem cells for redistribution in the body. The transformation of injectable cyborganics into cyborganic factories that can manufacture bone regenerative stem cells and biologics within the body is for obvious reasons a “sought-out-after” scenario in the treatment of systemic bone disorders. For now, however, our study has demonstrated that M2-based cyborganic carriers could potentially augment healing of fractured bones; nevertheless, *in vivo* studies are needed to fully support this assumption, and to understand to what degree these carriers could reduce the risk of osteoporotic fractures and reduce the use of external fracture stability devices (cast or surgical fixation) in fracture treatment. Furthermore, such *in vivo* studies will also enable us to test whether M2 carriers can transform into cyborganic factories that stimulate stem cells to treat systemic bone diseases through the generation of new regenerative factors. We further envision that nanoelectronic inclusion into such clay-based hydrogels can pave the way for wireless monitoring of the bone

repair, which could also be used for a controlled secretion of regenerative agents at the target site. Moreover, we also envision that the inclusion of osteoclast cells in our systems could better elucidate the potential of these hydrogel carriers to reverse the bone formation imbalance in osteoporotic patients.

CONCLUSIONS

We have successfully utilized a combinatorial approach to identify a hydrogel made from polysaccharide-based biopolymers and MMT clay nanomaterials. Our hydrogel library consisted of 63 samples with varying polymer compositions and inputs that exhibited different mechanical and biological properties. We identified a hydrogel made from a hydrogel-MMT composition that strongly interacted with the polyanionic polymer matrix and improved a range of physical and biological properties of the pristine hydrogel. Specifically, this optimal combination could transform an otherwise brittlelike hydrogel into a shear-thinning, load-bearing, shock-absorbing, and osteogenic hydrogel. The MMT-based hydrogel also enables hMSCs to deposit a mature bonelike matrix consisting of differentiated cells and crystalline apatite without being exposed to any additional differentiation conditions. Notably, we found a 36-fold increase in ALP and a 11-fold increase in the formation of mineralized matrix for M2—compared to our control hydrogel (C1—). To find this combination, we had to screen approximately 63 hydrogels that had different mechanical, chemical, and biological properties. To this end, we argued that the identified hit combination could perform these regenerative tasks due to a perfect combination of hydrogel stiffness and mineral composition. We have no doubt that this is in part due to the combinatorial approach used in this study.

MATERIALS AND METHODS

Nanocomposite Hydrogel Fabrication. A wide selection of combinatorial hydrogels was prepared using thiol-modified hyaluronic acid (HA, Gycosil from HyStem Hydrogel Kit, ESI BIO), 8-arm PEG-acrylate (8PEGA, MW = 10 kDa, Creative PEGworks), alginate (AL, pharmaceutical grade, FMC Biopolymer, U.K.), various nanoclays (Laponite RD (LAP, BYK, U.K.)), Montmorillonite (MMT, BYK), and Sumecton (SUM, Kunimine Industries Co., Ltd., Japan). Initially, a stock solution of 1.1% (w/v) HA was prepared in deionized water and mixed with a 4% (w/v) Al solution to reach the targeted HA–Al ratio. This solution was magnetically stirred overnight, whereafter different nanoclays were gently added to the respective solutions and allowed to dissolve and exfoliate overnight. To this end, the final concentrations (w/v) of HA and 8PEGA were always kept at 0.5 and 0.8%, respectively.

To prepare hydrogels without Al, the HA prepolymer solution was mixed with 8PEGA, and, to prepare nanoclay composites without Al, HA prepolymer was first mixed with an appropriate amount of clay prior to the addition of 8PEGA. This mix was allowed to incubate for 15 min to obtain a stable hydrogel. Similarly, to prepare hydrogels containing Al, a HA–Al solution (with clay, in case of nanoclay composite) was prepared prior to the addition of 8PEGA. This mix was also incubated overnight and rigorously stirred to enable the two polymers to mix properly. Afterward, 8PEGA was added to the mixture, and following the HA cross-linking, a 2% calcium chloride (CaCl₂) solution was added to cross-link the Al prepolymer ionically and yield a double-bonded hydrogel. After cross-linking, all samples were washed multiple times with Dulbecco's phosphate-buffered saline (DPBS, Sigma-Aldrich, U.K.) and used for downstream studies. The sample codes and feed composition of all hydrogels are listed in Table S1.

Proton NMR (¹H NMR) Spectroscopic Characterization. The covalent bond formation between HA and 8PEGA was assessed using ¹H NMR spectroscopy for 8PEGA, thiolated HA, and HA–8PEGA. 8PEGA and thiolated HA were prepared in deuterated water (D₂O) at a concentration of 1% (w/v). However, HA–8PEGA was prepared using the same process as used for gel preparation and 1.1% (w/v) thiolated HA reacted with 0.8% (w/v) 8PEGA in D₂O inside the NMR tube. The ¹H NMR spectra were then recorded on a Varian Mercury 400 MHz spectrometer at 25 °C, using tetramethylsilane as the internal standard. All ¹H NMR spectra were obtained at a spectral width of 8012.82 Hz and an acquisition time of 8.18 s; 131 072 data points were collected under 6.5 ms pulse; and the chemical shifts (δ) are reported in parts per million (ppm) relative to the solvent signal peak.

Fourier Transform Infrared (FTIR) Spectroscopy Analysis. The prepared hydrogels were washed multiple times with deionized water and lyophilized for 48 h before analysis. FTIR spectra were recorded using a PerkinElmer Spectrum 100 FTIR spectrometer equipped with a diamond crystal attenuated total reflectance accessory after background subtraction. The transmittance spectra of the lyophilized hydrogels were collected over the range of 4000–500 cm⁻¹ with 16 scans at a resolution of 4 cm⁻¹. All spectra were baseline-corrected and normalized using the PerkinElmer Spectrum software. Each sample was measured at four different parts, and the averaged spectra were used for the analysis.

X-ray Powder Diffraction (XRD) Analysis. The hydrogel samples were prepared as described in the previous section. XRD analysis was performed using a HUBER G670 X-ray powder diffractometer (Germany) employing the image plate detection method in the Guinier geometry. The analysis was performed in the 2θ range of 10–80° at a step size of 0.005°, and the diffractometer was equipped with secondary monochrome and Cu X-ray tube. The sealed tube X-ray generator was operated at 40 kV and 40 mA to provide Cu Kα₁ radiations of wavelength 1.54056 Å.

ζ-Potential Measurements. ζ-Potential of the various polymer solutions was measured on a Malvern Zetasizer apparatus (Nano Series ZS, Malvern Instruments, Worcestershire, U.K.) equipped with a 4 mW He–Ne laser operating at 632.8 nm, at 25 °C. The

prepolymer solutions were diluted 10 times in deionized water and measured. The nanoclays were dispersed using a vortexer and ultrasonicated for 5 min prior to the measurements of the ζ-potential of the clays.

Scanning Electron Microscopy (SEM) and Energy-Dispersive X-ray Spectroscopy Analysis (EDAX). To determine the porosity of the hydrogels and examine the apatite formation within them, SEM and EDAX were used. The hydrogels were washed, lyophilized for 48 h, and cross-sectioned. Then, the cross-sectional images were acquired with SEM (FEI Quanta 200 ESEM FEG) operating at an accelerating voltage of 10 kV. All samples were sputter-coated with gold (10 nm) before SEM imaging. ImageJ was used to measure the pore size of the captured SEM images. The average pore size was calculated from at least 40 independent measurements for each sample. The EDAX measurements were performed for the same samples prior to the gold sputtering by utilizing an energy-dispersive X-ray spectrometer (EDX; Oxford Instruments 80 mm² X-Max silicon drift detector) connected to the SEM instrument. All elemental compositions were recorded in weight percentage, and the respective Ca/P ratio was calculated by dividing the calcium weight percentage by that of phosphorus.

Degradation and Swelling Study. To assess the degradation rate and swelling behavior, the hydrogels were incubated in PBS at 37 °C for approximately 2 h. Afterward, the wet weight (*M_w*) of the hydrogels was recorded at 8, 12, 16, 36, 84, and 168 h of incubation. The mass remaining (%) was then calculated using eq 1, where the mass of the respective samples at each time point (*M_w(t)*) was divided by its measured weight at 8 h. Each combination was replicated four times to get an average value of the remaining mass (%).

$$\text{mass remaining (\%)} = \frac{M_w(t)}{M_w(8\text{ h})} \times 100 \quad (1)$$

To measure the swelling ratio, the wet weight (*M_w*) and dry weight (*M_d*) of each hydrogel were measured at the respective time points. The swelling ratio was then calculated using eq 2. At least four samples were studied for each combination.

$$\text{swelling ratio} = \frac{M_w - M_d}{M_d} \quad (2)$$

Mechanical Characterization. The mechanical properties of the hydrogels were analyzed using an Instron (model 5967, U.K.) mechanical tester equipped with a 50 N load cell, under a compression rate of 0.5 mm/min. For compression testing, the hydrogels were prepared in Teflon molds with a uniform cylindrical shape (5 mm diameter × 10 mm depth). Following polymer cross-linking, the hydrogels were incubated in DPBS overnight at 37 °C. Prior to the test, the diameter and height of the hydrogels were measured using a Vernier caliper. The compressive modulus was calculated from the slope of the stress–strain curve in the 15–25% strain region. To calculate the toughness and recovery of the hydrogels, three complete compression–recovery cycles until 50% strain were performed at a rate of 0.5 mm/min. The toughness was estimated as the area under the stress–strain curve, while recovery (%) was calculated as the ratio of toughness in the third and second recovery cycles (eq 3).

$$\text{recovery}_{2 \rightarrow 3} (\%) = \frac{\text{toughness (3}^{\text{rd}} \text{ cycle)}}{\text{toughness (2}^{\text{nd}} \text{ cycle)}} \times 100 \quad (3)$$

Energy dissipation of each complete cycle was calculated using eq 4 by measuring the area in between the loading and unloading hysteresis curves, using Matlab mathematic toolbox software (MathWorks, Natick, MA).

$$\text{energy dissipation} = \text{toughness (loading)} - \text{toughness (unloading)} \quad (4)$$

Rheological Study. The rheological properties of the polymers were assessed with a Discovery Hybrid Rheometer HR-2 (TA

Instruments) at 25 °C. The gelation kinetics and shear-thinning behavior of the prepolymer solutions was studied using a 25 mm parallel plate geometry at a gap distance of 300 μm . The solutions were mixed for 10 s and immediately tested. The shear-thinning property was investigated using a flow sweep test performed over a range of shear rates ($0.1\text{--}10^3\text{ s}^{-1}$). The gelation time was estimated from an oscillation time test performed at 1% strain and an angular frequency of 50 rad/s.

Human Mesenchymal Stem Cell Culture. Human bone marrow-derived mesenchymal stem cells (hMSCs) (Lonza Inc.) were used at passage 3–4 for all cell viability and differentiation studies except for the push-out test and DAPI staining experiments where the cells were encapsulated at passage 5. hMSC suspension was mixed with the respective prepolymer solution before the addition of 8PEGA. Immediately after the addition of 8PEGA, this hMSC-laden prepolymer solution was deposited into a microwell array (2 mm diameter \times 1 mm depth, Grace Bio-Labs) mounted on a glass slide using an automatic pipette (Eppendorf Xplorer, H31141F, Eppendorf, Germany). The solution was allowed to polymerize for 10 min at 37 °C.

The solutions containing Al were further cross-linked by layering the hydrogel with 50 μL of 2% CaCl_2 solution for 5 min. After cross-linking, the cell-laden hydrogels were washed twice with DPBS and cultured in mesenchymal stem cell basal medium (MSCBM, Lonza) supplemented with MSCGM SingleQuots (PT-410S, Lonza). The MSCGM SingleQuots contained mesenchymal cell growth supplement (MCGS), L-glutamine, and GA-1000. The culture medium was changed with either fresh MSCBM or differentiation media the next day, and afterward, the cells were fed every 3–5 days. The differentiation medium was prepared by supplementing the osteogenic basal medium (PT-3924, Lonza) with hMSC osteogenic SingleQuots (PT-4120, Lonza) containing dexamethasone, L-glutamine, ascorbate, MCGS, penicillin/streptomycin, and β -glycerophosphate. In the stem cell differentiation study, the cellular concentration per hydrogel was 2.5×10^6 cells/mL, whereas in the push-out test, 10×10^6 cells/mL were used.

Live/Dead Viability Assay. To evaluate the hydrogel cytotoxicity, hMSCs were encapsulated at a final concentration of 10^6 cells/mL and stained on days 1, 5, 7, and 14 using a Live/Dead viability assay (Life Technologies) according to the manufacturer's protocol. The live cells (stained with Calcein-AM) and the dead cells (stained with ethidium homodimer-1) were imaged using a confocal laser scanning microscope (CLSM, Zeiss LSM 700, Germany) and analyzed using ImageJ (National Institutes of Health). To quantify the viability, the images were split into green and red channels to count for live and dead cells, respectively. The live cell count and dead cell count were combined to obtain the total cell count within the hydrogels. Finally, the cell viability (%) was calculated according to the following equation

$$\text{viability (\%)} = \frac{\text{live cell count}}{\text{total cell count}} \times 100 \quad (5)$$

DAPI Staining. A 4,6-diamidino-2-phenylindole dilactate (DAPI, NucBlue Live ReadyProbes Reagent, Molecular Probes) was used to counterstain the nucleus of the cells incubated within hydrogels for 14 and 21 days. First, the hydrogels were washed with DPBS and fixed in 4% formaldehyde (Thermo Fisher) for 20 min. Next, the cells were incubated in 0.15% (v/v, in DPBS) Triton X-100 solution for 20 min to allow membrane permeabilization. Finally, the hydrogels were incubated in DAPI solution for 30 min at room temperature, washed with DPBS multiple times, and imaged using a confocal laser scanning microscope (Zeiss LSM 700, Germany). At least eight samples were stained for each condition, and the number of cell nuclei within the gels was counted using built-in functions in ImageJ (National Institutes of Health).

Alkaline Phosphatase (ALP) Staining and Activity. The intracellular alkaline phosphatase (ALP) activity of the hMSCs was assessed by utilizing a 5-bromo-4-chloro-3-indolyl phosphate/nitro blue tetrazolium (BCIP/NBT, Thermo Fisher Scientific) solution. First, the cell-laden hydrogels were washed three times with DPBS

covered with BCIP/NBT and incubated in a light-protective environment at room temperature for 2 h. Then, the hydrogels were washed three times with DPBS to remove excess BCIP/NBT and imaged in bright field with a Zeiss AxioScope 40 microscope (Carl Zeiss, Germany). However, the hydrogels containing Al were first treated with 1.6 M sodium citrate solution for 12 h to remove the opaque (white) background of the hydrogels by cleaving the ionic linkages between alginate chains. The ALP expression was estimated from the area covered by the black-violet stained cells by applying a manual threshold and a series of built-in modules of CellProfiler. Finally, the ALP expression of each condition was normalized to the ALP expression in C1 hydrogels.

The ALP activity was also evaluated spectrophotometrically by Alkaline Phosphatase Assay Kit (ab83369, Abcam, U.K.), as suggested in the manufacturer's protocol. Briefly, the hydrogels were digested in a hyaluronidase solution (115 μL , 5 mg/mL, Sigma-Aldrich) at 37 °C for 24 h. After hydrogel digestion, 10% (v/v) Triton X-100 solution was added to the respective solutions to reach a final concentration of 0.1%. The solution was centrifuged for 1 min to remove any insoluble material. Finally, the supernatant was mixed with an assay buffer solution within a 96-well plate and combined with an ALP substrate (5 mM pNPP), which ALP can cleave to generate a yellowish color that is detectable by a spectrophotometer. Specifically, we quantified the concentration of the cleaved substrate by measuring the absorbance (OD) at 405 nm after 2 h with a microplate reader (Victor, PerkinElmer) and normalizing to C1– condition.

Alizarin Red S Staining. Bone mineralization in the cell-laden hydrogels was assessed in terms of extracellular calcium deposition by Alizarin Red S (ARED) staining. The staining solution was prepared by dissolving 1 g of ARED powder (Sigma-Aldrich) in 50 mL of DPBS (without CaCl_2 and MgCl_2). To achieve a complete ARED dissolution, the pH of the staining solution was adjusted to 4.2 ± 0.1 . Finally, the ARED staining solution was filtered through a 0.45 μm syringe filter (Frisenette ApS, Denmark).

Prior to staining, the cells within the hydrogels were fixed in a 4% formaldehyde solution for 30 min. Then, the hydrogels were washed in DPBS and incubated in the ARED solution for 1 h at room temperature in a light-protected environment. After staining, the hydrogels were washed repeatedly with DPBS for 5 h to remove any unspecific ARED binding and subsequently imaged in bright field on a Zeiss AxioScope 40 microscope (Carl Zeiss, Germany). The mean intensities of the images were measured using built-in functions of ImageJ (National Institutes of Health) as an estimation of osteoblast-mediated mineralization. Finally, the measured mean intensity of each condition was normalized to the mean staining intensity of C1– hydrogels.

Calcium Detection. The calcified deposition within the ECM of the cell-laden hydrogels was quantified using a colorimetric calcium detection assay kit (ab102505, Abcam) as per the manufacturer's protocol. Specifically, a chromogenic complex formed between free calcium ions and o-cresolphthalein, which was measurable through spectrophotometry at a wavelength of 575 nm. Briefly, the hydrogels were digested in an alginate lyase solution (45 μL , 1 mg/mL, Sigma-Aldrich, Japan) by vortexing for 1 min at 37 °C in hyaluronidase (45 μL , 5 mg/mL, Sigma-Aldrich). After complete digestion of the hydrogels, a solution of Triton X-100 (1% in 2.5 M HCl) was added to reach the final concentration of 0.1%, and the mixture was vortexed for 1 min. Afterward, the solution was microcentrifuged for 1 min to remove any insoluble materials. Finally, the supernatant (50 μL) was mixed with a chromogenic reagent (90 μL) and assay buffer solution (60 μL) in a 96-well plate. After 10 min of incubation at room temperature, the absorbance at 575 nm was measured in a microplate reader (Victor, PerkinElmer).

Push-Out Test. The interfacial adhesion strength between the respective hydrogels and the artificial bone defects was investigated via a push-out test. To this end, a bovine femur was sliced to a thickness of 5 mm, and a 3.5 mm drill was used to create a defect in the middle of each bone slice. The defect sites were filled with cell-laden hydrogels and placed in a six-well plate containing either the growth medium or differentiation medium. After 5 weeks of

incubation, push-out test was carried out by using the Instron mechanical tester (5967 model) in indentation mode (3 mm probe). To this end, a 50 N load cell was used along with the indentation probe to push out the respective hydrogels at a rate of 0.5 mm/s.

Statistical Analysis. Statistical analysis was performed using GraphPad Prism 7 software (San Diego). All quantifications are presented as mean \pm standard deviation, unless stated otherwise. The significant differences between different data sets were determined through one-way analysis of variance, followed by Tukey's post hoc test in the case of a Gaussian distribution. However, for non-Gaussian distribution, nonparametric Dunn's multiple comparisons test was utilized, and finally, the statistical significance was defined as *($p < 0.05$), **($p < 0.01$), ***($p < 0.001$), and ****($p < 0.0001$).

■ ASSOCIATED CONTENT

● Supporting Information

The Supporting Information is available free of charge on the ACS Publications website at DOI: 10.1021/acsami.8b11436.

Rheological properties, ζ -potential, compositions of the hydrogels, ^1H NMR spectroscopy, and FTIR spectroscopy characterization of the nanocomposite systems; mechanical analysis of nanoreinforced HA- and Al hydrogels; effect of ionic cross-linking and 8PGEA on compressive modulus and toughness of hydrogels; variation of cell density vs time; FTIR spectra of the hydrogels with and without cells at different time points; SEM images and EDS analysis of cell-free nanocomposites after 6 weeks (PDF)

■ AUTHOR INFORMATION

Corresponding Authors

*E-mail: eng.mehrali@gmail.com (M.M.).

*E-mail: aldo@nanotech.dtu.dk (A.D.-P.).

ORCID

Ayyoob Arpanaei: 0000-0003-3872-2933

Akhilesh K. Gaharwar: 0000-0002-0284-0201

Alireza Dolatshahi-Pirouz: 0000-0001-6326-0836

Notes

The authors declare no competing financial interest.

■ ACKNOWLEDGMENTS

ADP acknowledges the Danish Council for Independent Research (Technology and Production Sciences, 5054-00142B), Gigtforeningen (R139-A3864), and the Villum Foundation (10103) for support. The authors also acknowledge "Haderer & Muller Biomedical Art" for creating the illustration presented in Figures 7, and 8, as well as for the graphical content figure.

■ REFERENCES

- (1) Liu, Y.; Lim, J.; Teoh, S. H. Review: Development of Clinically Relevant Scaffolds for Vascularised Bone Tissue Engineering. *Biotechnol. Adv.* **2013**, *31*, 688–705.
- (2) Shegarfi, H.; Reikeras, O. Review Article: Bone Transplantation and Immune Response. *J. Orthop. Surg.* **2009**, *17*, 206–211.
- (3) Phetfong, J.; Sanvoranart, T.; Nartprayut, K.; Nimsanor, N.; Seenprachawong, K.; Prachayasittikul, V.; Supokawej, A. Osteoporosis: The Current Status of Mesenchymal Stem Cell-Based Therapy. *Cell. Mol. Biol. Lett.* **2016**, *21*, No. 12.
- (4) Kiernan, J.; Hu, S.; Grynypas, M. D.; Davies, J. E.; Stanford, W. L. Systemic Mesenchymal Stromal Cell Transplantation Prevents Functional Bone Loss in a Mouse Model of Age-Related Osteoporosis. *Stem Cells Transl. Med.* **2016**, *5*, 683–693.

- (5) Aguado, B. A.; Mulyasmita, W.; Su, J.; Lampe, K. J.; Heilshorn, S. C. Improving Viability of Stem Cells During Syringe Needle Flow Through the Design of Hydrogel Cell Carriers. *Tissue Eng., Part A* **2012**, *18*, 806–815.

- (6) Agashi, K.; Chau, D. Y. S.; Shakesheff, K. M. The Effect of Delivery Via Narrow-Bore Needles on Mesenchymal Cells. *Regener. Med.* **2009**, *4*, 49–64.

- (7) Li, L.; Chen, X. W.; Wang, W. E.; Zeng, C. Y. How to Improve the Survival of Transplanted Mesenchymal Stem Cell in Ischemic Heart? *Stem Cells Int.* **2016**, *2016*, 1–14.

- (8) Parisi-Amon, A.; Mulyasmita, W.; Chung, C.; Heilshorn, S. C. Protein-Engineered Injectable Hydrogel to Improve Retention of Transplanted Adipose-Derived Stem Cells. *Adv. Healthcare Mater.* **2013**, *2*, 428–432.

- (9) Leslie, S. K.; Nicolini, A. M.; Sundaresan, G.; Zweit, J.; Boyan, B. D.; Schwartz, Z. Development of a Cell Delivery System Using Alginate Microbeads for Tissue Regeneration. *J. Mater. Chem. B* **2016**, *4*, 3515–3525.

- (10) Hoffman, M. D.; Xie, C.; Zhang, X. P.; Benoit, D. S. W. The Effect of Mesenchymal Stem Cells Delivered via Hydrogel-Based Tissue Engineered Periosteum on Bone Allograft Healing. *Biomaterials* **2013**, *34*, 8887–8898.

- (11) Thakur, A.; Jaiswal, M. K.; Peak, C. W.; Carrow, J. K.; Gentry, J.; Dolatshahi-Pirouz, A.; Gaharwar, A. K. Injectable Shear-Thinning Nanoengineered Hydrogels for Stem Cell Delivery. *Nanoscale* **2016**, *8*, 12362–12372.

- (12) Sun, J. Y.; Zhao, X. H.; Illeperuma, W. R. K.; Chaudhuri, O.; Oh, K. H.; Mooney, D. J.; Vlassak, J. J.; Suo, Z. G. Highly Stretchable and Tough Hydrogels. *Nature* **2012**, *489*, 133–136.

- (13) Mehrali, M.; Thakur, A.; Pennisi, C. P.; Talebian, S.; Arpanaei, A.; Nikkhah, M.; Dolatshahi-Pirouz, A. Nanoreinforced Hydrogels for Tissue Engineering: Biomaterials that are Compatible with Load-Bearing and Electroactive Tissues. *Adv. Mater.* **2017**, *29*, No. 1603612.

- (14) Gaharwar, A. K.; Patel, A.; Dolatshahi-Pirouz, A.; Zhang, H. B.; Rangarajan, K.; Iviglia, G.; Shin, S. R.; Hussain, M. A.; Khademhosseini, A. Elastomeric Nanocomposite Scaffolds Made from Poly(Glycerol Sebacate) Chemically Crosslinked with Carbon Nanotubes. *Biomater. Sci.* **2015**, *3*, 46–58.

- (15) Jensen, T.; Jakobsen, T.; Baas, J.; Nygaard, J. V.; Dolatshahi-Pirouz, A.; Hovgaard, M. B.; Foss, M.; Bungler, C.; Besenbacher, F.; Soballe, K. Hydroxyapatite Nanoparticles In Poly-D,L-Lactic Acid Coatings on Porous Titanium Implants Conducts Bone Formation. *J. Biomed. Mater. Res., Part A* **2010**, *95*, 665–672.

- (16) Mehrali, M.; Akhiani, A. R.; Talebian, S.; Mehrali, M.; Latibari, S. T.; Dolatshahi-Pirouz, A.; Metselaar, H. S. C. Electrophoretic Deposition of Calcium Silicate-Reduced Graphene Oxide Composites on Titanium Substrate. *J. Eur. Ceram. Soc.* **2016**, *36*, 319–332.

- (17) Mehra, M.; Asadollahi, M. A.; Nasri-Nasrabadi, B.; Ghaedi, K.; Salehi, H.; Dolatshahi-Pirouz, A.; Arpanaei, A. Incorporation of Mesoporous Silica Nanoparticles into Random Electrospun Plga and Plga/Gelatin Nanofibrous Scaffolds Enhances Mechanical and Cell Proliferation Properties. *Mater. Sci. Eng., C* **2016**, *66*, 25–32.

- (18) Su, D.; Jiang, L. B.; Chen, X.; Dong, J.; Shao, Z. Z. Enhancing the Gelation and Bioactivity of Injectable Silk Fibroin Hydrogel with Laponite Nanoplatelets. *ACS Appl. Mater. Interfaces* **2016**, *8*, 9619–9628.

- (19) Thorpe, A. A.; Creasey, S.; Sammon, C.; Le Maitre, C. L. Hydroxyapatite Nanoparticle Injectable Hydrogel Scaffold to Support Osteogenic Differentiation of Human Mesenchymal Stem Cells. *Eur. Cells Mater.* **2016**, *32*, 1–23.

- (20) Jensen, T.; Dolatshahi-Pirouz, A.; Foss, M.; Baas, J.; Lovmand, J.; Duch, M.; Pedersen, F. S.; Kassem, M.; Bungler, C.; Soballe, K.; Besenbacher, F. Interaction of Human Mesenchymal Stem Cells with Osteopontin Coated Hydroxyapatite Surfaces. *Colloids Surf., B* **2010**, *75*, 186–193.

- (21) Xavier, J. R.; Thakur, T.; Desai, P.; Jaiswal, M. K.; Sears, N.; Cosgriff-Hernandez, E.; Kaunas, R.; Gaharwar, A. K. Bioactive

Nanoengineered Hydrogels for Bone Tissue Engineering: A Growth-Factor-Free Approach. *ACS Nano* **2015**, *9*, 3109–3118.

(22) Dvir, T.; Timko, B. P.; Brigham, M. D.; Naik, S. R.; Karajanagi, S. S.; Levy, O.; Jin, H. W.; Parker, K. K.; Langer, R.; Kohane, D. S. Nanowired Three-Dimensional Cardiac Patches. *Nat. Nanotechnol.* **2011**, *6*, 720–725.

(23) Feiner, R.; Dvir, T. Tissue-Electronics Interfaces: from Implantable Devices to Engineered Tissues. *Nat. Rev. Mater.* **2018**, *3*, No. 17076.

(24) Tian, B.; Liu, J.; Dvir, T.; Jin, L. H.; Tsui, J. H.; Qing, Q.; Suo, Z. G.; Langer, R.; Kohane, D. S.; Lieber, C. M. Macroporous Nanowire Nanoelectronic Scaffolds for Synthetic Tissues. *Nat. Mater.* **2012**, *11*, 986–994.

(25) Fakhari, A.; Berkland, C. Applications and Emerging Trends of Hyaluronic Acid in Tissue Engineering, as a Dermal Filler and in Osteoarthritis Treatment. *Acta Biomater.* **2013**, *9*, 7081–7092.

(26) Weissmann, B.; Meyer, K. Structure of Hyaluronic Acid - the Glucuronic Linkage. *J. Am. Chem. Soc.* **1952**, *74*, 4729.

(27) Macdougall, L. J.; Truong, V. X.; Dove, A. P. Efficient In Situ Nucleophilic Thiol-yne Click Chemistry for the Synthesis of Strong Hydrogel Materials with Tunable Properties. *ACS Macro Lett.* **2017**, *6*, 93–97.

(28) Li, J. Y.; Illeperuma, W. B. K.; Suo, Z. G.; Vlassak, J. J. Hybrid Hydrogels with Extremely High Stiffness and Toughness. *ACS Macro Lett.* **2014**, *3*, 520–523.

(29) Kennedy, R.; Hassan, W. U.; Tochwin, A.; Zhao, T.; Dong, Y.; Wang, Q.; Tai, H.; Wang, W. In Situ Formed Hybrid Hydrogels from Peg Based Multifunctional Hyperbranched Copolymers: a Raft Approach. *Polym. Chem.* **2014**, *5*, 1838–1842.

(30) Jain, E.; Hill, L.; Canning, E.; Sell, S. A.; Zusiak, S. P. Control of Gelation, Degradation and Physical Properties of Polyethylene Glycol Hydrogels Through the Chemical and Physical Identity of the Crosslinker. *J. Mater. Chem. B* **2017**, *5*, 2679–2691.

(31) Nguyen, M. K.; Jeon, O.; Krebs, M. D.; Schapira, D.; Alsborg, E. Sustained localized Presentation of RNA Interfering Molecules from in Situ Forming Hydrogels to Guide Stem Cell Osteogenic Differentiation. *Biomaterials* **2014**, *35*, 6278–6286.

(32) Carrion, B.; Souzanchi, M. F.; Wang, V. T.; Tiruchinapally, G.; Shikanov, A.; Putnam, A. J.; Coleman, R. M. The Synergistic Effects of Matrix Stiffness and Composition on the Response of Chondroprogenitor Cells in a 3D Precondensation Microenvironment. *Adv. Healthcare Mater.* **2016**, *5*, 1192–1202.

(33) Ji, Y.; Ghosh, K.; Li, B.; Sokolov, J. C.; Clark, R. A.; Rafailovich, M. H. Dual-Syringe Reactive Electrospinning of Cross-Linked Hyaluronic Acid Hydrogel Nanofibers for Tissue Engineering Applications. *Macromol. Biosci.* **2006**, *6*, 811–817.

(34) Chung, S.; Lee, H.; Kim, H.-S.; Kim, M.-G.; Lee, L. P.; Lee, J. Y. Transdermal Thiol-Acrylate Polyethylene Glycol Hydrogel Synthesis Using Near Infrared Light. *Nanoscale* **2016**, *8*, 14213–14221.

(35) Voo, W.-P.; Lee, B.-B.; Idris, A.; Islam, A.; Tey, B.-T.; Chan, E.-S. Production of Ultra-High Concentration Calcium Alginate Beads with Prolonged Dissolution Profile. *RSC Adv.* **2015**, *5*, 36687–36695.

(36) Treenate, P.; Monvisadee, P. Crosslinker Effects on Properties of Hydroxyethylacryl Chitosan/Sodium Alginate Hydrogel Films. *Macromolecular Symposia*; Wiley Online Library, 2017; pp 147–153.

(37) Qi, X.; Guan, Y.; Chen, G.; Zhang, B.; Ren, J.; Peng, F.; Sun, R. A Non-Covalent Strategy for Montmorillonite/Xylose Self-Healing Hydrogels. *RSC Adv.* **2015**, *5*, 41006–41012.

(38) Karageorgiou, V.; Kaplan, D. Porosity of 3D Biomaterial Scaffolds and Osteogenesis. *Biomaterials* **2005**, *26*, 5474–5491.

(39) Camci-Unal, G.; Cuttica, D.; Annabi, N.; Demarchi, D.; Khademhosseini, A. Synthesis and Characterization of Hybrid Hyaluronic Acid-Gelatin Hydrogels. *Biomacromolecules* **2013**, *14*, 1085–1092.

(40) Das, P.; Malho, J. M.; Rahimi, K.; Schacher, F. H.; Wang, B. C.; Demco, D. E.; Walther, A. Nacre-Mimetics with Synthetic Nanoclays Up to Ultrahigh Aspect Ratios. *Nat. Commun.* **2015**, *6*, No. 5967.

(41) Humphrey, J. D.; Dufresne, E. R.; Schwartz, M. A. Mechanotransduction and Extracellular Matrix Homeostasis. *Nat. Rev. Mol. Cell Biol.* **2014**, *15*, 802–812.

(42) Huebsch, N.; Lippens, E.; Lee, K.; Mehta, M.; Koshy, S. T.; Darnell, M. C.; Desai, R. M.; Madl, C. M.; Xu, M.; Zhao, X. H.; Chaudhuri, O.; Verbeke, C.; Kim, W. S.; Alim, K.; Mammoto, A.; Ingber, D. E.; Duda, G. N.; Mooney, D. J. Matrix Elasticity of Void-Forming Hydrogels Controls Transplanted-Stem-Cell-Mediated Bone Formation. *Nat. Mater.* **2015**, *14*, 1269–1277.

(43) Gaharwar, A. K.; Schexnailder, P. J.; Kline, B. P.; Schmidt, G. Assessment of Using Laponite (R) Cross-Linked Poly(Ethylene Oxide) for Controlled Cell Adhesion and Mineralization. *Acta Biomater.* **2011**, *7*, 568–577.

(44) Burdick, J. A.; Prestwich, G. D. Hyaluronic Acid Hydrogels for Biomedical Applications. *Adv. Mater.* **2011**, *23*, H41–H56.

(45) Guermani, E.; Shaki, H.; Mohanty, S.; Mehrali, M.; Arpanaei, A.; Gaharwar, A. K.; Dolatshahi-Pirouz, A. Engineering Complex Tissue-Like Microgel Arrays for Evaluating Stem Cell Differentiation. *Sci. Rep.* **2016**, *6*, No. 30445.

(46) Venkatesan, J.; Bhatnagar, I.; Manivasagan, P.; Kang, K. H.; Kim, S. K. Alginate Composites for Bone Tissue Engineering: A Review. *Int. J. Biol. Macromol.* **2015**, *72*, 269–281.

(47) Gaharwar, A. K.; Mihaila, S. M.; Swami, A.; Patel, A.; Sant, S.; Reis, R. L.; Marques, A. P.; Gomes, M. E.; Khademhosseini, A. Bioactive Silicate Nanoplatelets for Osteogenic Differentiation of Human Mesenchymal Stem Cells. *Adv. Mater.* **2013**, *25*, 3329–3336.

(48) Gaharwar, A. K.; Arpanaei, A.; Andresen, T. L.; Dolatshahi-Pirouz, A. 3D Biomaterial Microarrays for Regenerative Medicine: Current State-of-the-Art, Emerging Directions and Future Trends. *Adv. Mater.* **2016**, *28*, 771–781.

(49) Gaharwar, A. K.; Mukundan, S.; Karaca, E.; Dolatshahi-Pirouz, A.; Patel, A.; Rangarajan, K.; Mihaila, S. M.; Iviglia, G.; Zhang, H.; Khademhosseini, A. Nanoclay-Enriched Poly(Varepsilon-Caprolactone) Electrospun Scaffolds for Osteogenic Differentiation of Human Mesenchymal Stem Cells. *Tissue Eng., Part A* **2014**, *20*, 2088–2101.

(50) Dolatshahi-Pirouz, A.; Nikkha, M.; Kolind, K.; Dokmeci, M. R.; Khademhosseini, A. Micro- and Nanoengineering Approaches to Control Stem Cell-Biomaterial Interactions. *J. Funct. Biomater.* **2011**, *2*, 88–106.

(51) Kolind, K.; Dolatshahi-Pirouz, A.; Lovmand, J.; Pedersen, F. S.; Foss, M.; Besenbacher, F. A Combinatorial Screening of Human Fibroblast Responses on Micro-Structured Surfaces. *Biomaterials* **2010**, *31*, 9182–9191.

(52) Guo, P.; Shi, Z. L.; Liu, A.; Lin, T.; Bi, F.; Shi, M.; Yan, S. G. Effects of Cartilage Oligomeric Matrix Protein on Bone Morphogenetic Protein-2-Induced Differentiation of Mesenchymal Stem Cells. *Orthop. Surg.* **2014**, *6*, 280–287.

(53) Shahabi, S.; Najafi, F.; Majdabadi, A.; Hooshmand, T.; Nazarpak, M. H.; Karimi, B.; Fatemi, S. M. Effect of Gamma Irradiation on Structural and Biological Properties of a PLGA-PEG-Hydroxyapatite Composite. *Sci. World J.* **2014**, *2014*, 1–9.

(54) Chen, W.; Long, T.; Guo, Y. J.; Zhu, Z. A.; Guo, Y. P. Hydrothermal Synthesis of Hydroxyapatite Coatings with Oriented Nanorod Arrays. *RSC Adv.* **2014**, *4*, 185–191.

(55) Ambre, A. H.; Katti, D. R.; Katti, K. S. Nanoclays Mediate Stem Cell Differentiation and Mineralized Ecm Formation on Biopolymer Scaffolds. *J. Biomed. Mater. Res., Part A* **2013**, *101*, 2644–2660.

(56) Chavan, P. N.; Bahir, M. M.; Mene, R. U.; Mahabole, M. P.; Khairnar, R. S. Study of Nanobiomaterial Hydroxyapatite in Simulated Body Fluid: Formation and Growth Of Apatite. *Mater. Sci. Eng., B* **2010**, *168*, 224–230.

(57) An, Y. H.; Draughn, R. A. *Mechanical Testing of Bone and the Bone-Implant Interface*; CRC Press: Boca Raton, 2000; p 624.

(58) Hong, S. M.; Sycks, D.; Chan, H. F.; Lin, S. T.; Lopez, G. P.; Guilak, F.; Leong, K. W.; Zhao, X. H. 3D Printing of Highly Stretchable and Tough Hydrogels into Complex, Cellularized Structures. *Adv. Mater.* **2015**, *27*, 4035–4040.

(59) Wang, Q.; Mynar, J. L.; Yoshida, M.; Lee, E.; Lee, M.; Okuro, K.; Kinbara, K.; Aida, T. High-Water-Content Mouldable Hydrogels

by Mixing Clay and A Dendritic Molecular Binder. *Nature* **2010**, *463*, 339–343.

(60) Mieszawska, A. J.; Llamas, J. G.; Vaiana, C. A.; Kadakia, M. P.; Naik, R. R.; Kaplan, D. L. Clay Enriched Silk Biomaterials for Bone Formation. *Acta Biomater.* **2011**, *7*, 3036–3041.

(61) Mauro, N.; Chiellini, F.; Bartoli, C.; Gazzarri, M.; Laus, M.; Antonioli, D.; Griffiths, P.; Manfredi, A.; Ranucci, E.; Ferruti, P. Rgd-Mimic Polyamidoamine-Montmorillonite Composites with Tunable Stiffness as Scaffolds for Bone Tissue-Engineering Applications. *J. Tissue Eng. Regen. Med.* **2017**, *11*, 2164–2175.

(62) Gaharwar, A. K.; Peppas, N. A.; Khademhosseini, A. Nanocomposite Hydrogels for Biomedical Applications. *Biotechnol. Bioeng.* **2014**, *111*, 441–453.

(63) Zhang, F.; Phiel, C. J.; Spece, L.; Gurvich, N.; Klein, P. S. Inhibitory Phosphorylation of Glycogen Synthase Kinase-3 (Gsk-3) in Response to Lithium - Evidence for Autoregulation Of Gsk-3. *J. Biol. Chem.* **2003**, *278*, 33067–33077.

(64) Yoshizawa, S.; Brown, A.; Barchowsky, A.; Sfeir, C. Magnesium Ion Stimulation of Bone Marrow Stromal Cells Enhances Osteogenic Activity, Simulating the Effect Of Magnesium Alloy Degradation. *Acta Biomater.* **2014**, *10*, 2834–2842.

(65) Carrow, J. K.; Cross, L. M.; Reese, R. W.; Jaiswal, M. K.; Gregory, C. A.; Kaunas, R.; Singh, I.; Gaharwar, A. K. Widespread Changes in Transcriptome Profile of Human Mesenchymal Stem Cells Induced by Two-Dimensional Nanosilicates. *Proc. Natl. Acad. Sci. U.S.A.* **2018**, *115*, E3905–E3913.

(66) Schwarz, K.; Milne, D. B. Growth-Promoting Effects of Silicon in Rats. *Nature* **1972**, *239*, No. 333.

(67) Jugdaohsingh, R. Silicon and Bone Health. *J. Nutr., Health Aging* **2007**, *11*, 99–110.

(68) Reffitt, D. M.; Ogston, N.; Jugdaohsingh, R.; Cheung, H. F. J.; Evans, B. A. J.; Thompson, R. P. H.; Powell, J. J.; Hampson, G. N. Orthosilicic acid stimulates collagen type 1 synthesis and osteoblastic differentiation in human osteoblast-like cells in vitro. *Bone* **2003**, *32*, 127–135.

(69) Shin, S. R.; Aghaei-Ghareh-Bolagh, B.; Gao, X. G.; Nikkhah, M.; Jung, S. M.; Dolatshahi-Pirouz, A.; Kim, S. B.; Kim, S. M.; Dokmeci, M. R.; Tang, X. W.; Khademhosseini, A. Layer-by-Layer Assembly of 3D Tissue Constructs with Functionalized Graphene. *Adv. Funct. Mater.* **2014**, *24*, 6136–6144.

(70) Feiner, R.; Dvir, T. Engineered Hybrid Cardiac Patches With Multifunctional Electronics For Online Monitoring And Regulation Of Tissue Function. *Tissue Eng., Part A* **2016**, *22*, S54.